Elasto-plastic and hydromechanical models of failure around an infinitely long magma chamber,

Muriel Gerbault, Frédéric Cappa, R. Hassani

Geochemistry Geophysics Geosystems G3

Article
Volume 13, Number 3
13 March 2012
Q03009, doi:10.1029/2011GC003917
ISSN: 1525-2027

Published by AGU and the Geochemical Society

Elasto-plastic and hydromechanical models of failure around an infinitely long magma chamber

Muriel Gerbault, Frederic Cappa, and Riad Hassani

Géoazur, Université de Nice Sophia-Antipolis, Institut de Recherche pour le Développement (UR 082), Observatoire de la Côte d'Azur, 250 av Einstein, F-06560 Valbonne, France (gerbault@geoazur.unice.fr)

[1] Surface displacements solutions of elastic deformation around an inflating magma chamber generally assume that the associated internal overpressure is limited by the bedrock tensile strength. When considering stress equilibrium in the bedrock adjacent to a spherical or infinitely long cylinder, the gravity body force actually resists tensile failure, thus leading to a much larger pressure threshold. And when considering a Coulomb failure criterion, analytical and numerical models predict that shear failure develops instead of tensile failure. Here, three numerical codes are used to compare elasto-plastic solutions of surface displacements and patterns of failure in plane-strain. Shear failure propagates independently from the surface downward, then from the chamber walls upwards, and finally the two plasticized domains connect. Another test with internal underpressure (simulating source deflation) fits standard solutions from tunneling engineering. The effect of pore fluid pressures is also explored. In case of lithostatic fluid pore pressure in the bedrock, the gravity effect cancels out, and tensile failure is enabled for an overpressure close to the tensile strength. Coupled hydromechanical models in undrained conditions indicate that the initial bedrock porosity modifies the evolution of fluid pressure, volumetric strain and effective normal stress, and consequently also the pressure threshold for the onset of failure. We show that a bedrock of low porosity is more prone to fail than a bedrock of high porosity. In summary, our elasto-plastic and hydromechanical models illustrate the contexts for either tensile or shear failure around magmatic bodies, at the same time complementing and delimiting predictions deduced from elasticity.

Components: 13,100 words, 12 figures, 2 tables.

Keywords: eruption mechanisms; volcano monitoring.

Index Terms: 8118 Tectonophysics: Dynamics and mechanics of faulting (8004); 8414 Volcanology: Eruption mechanisms and flow emplacement; 8419 Volcanology: Volcano monitoring (4302, 7280).

Received 13 October 2011; **Revised** 9 January 2012; **Accepted** 19 January 2012; **Published** 13 March 2012.

Gerbault, M., F. Cappa, and R. Hassani (2012), Elasto-plastic and hydromechanical models of failure around an infinitely long magma chamber, *Geochem. Geophys. Geosyst.*, *13*, Q03009, doi:10.1029/2011GC003917.

1. Introduction

[2] Elastic deformation and failure resulting from an inflating magma chamber have been among the first analytical developments applied to geological observations [*Anderson*, 1936]. While a variety of magma sources shapes are considered when studying deformation associated to volcanism (e.g., see review by *Segall* [2009]), the heterogeneity of the medium, densities, thermal and viscous

properties are also well-known first order factors [e.g., *Tait et al.*, 1989; *Dragoni and Magnanensi*, 1989; *Parfitt et al.*, 1993; *Sartoris et al.*, 1990; *Trasatti et al.*, 2005; *Gudmundsson*, 2006; *Masterlark*, 2007; *Bonafede and Ferrari*, 2009; *Long and Grosfils*, 2009; *Karlstrom et al.*, 2010]. However, a first reference approach consists in considering an idealized circular or spherical cavity, submitted to uniform internal pressure in a homogeneous isotropic elastic half-space. Analytical solutions of this problem in two-dimensions (2D plane-strain) had been calculated in the 1920s by *Jeffery* [1921], who provided the stress distribution at the boundaries of a cavity and the free surface above it. This solution has been used to study dike intrusions around cylindrical magmatic chambers [e.g., *Gudmundsson*, 1988, 2006], or the influence of a volcanic edifice on conditions for eruption [e.g., *Pinel and Jaupart*, 2005]. The three-dimensional (3D) solution derived by *Mogi* [1958] for a pressure point source, further generalized by *McTigue* [1987], is also very much used today to evaluate changes in shape of active volcanic sources [e.g., *Battaglia et al.*, 2003; *Bonaccorso et al.*, 2005; *Pritchard and Simons*, 2004; *Masterlark*, 2007; *Segall*, 2009].

[3] Two conceptual approaches exist when considering how failure initiates from magmatic reservoirs. A first popular view, resulting from the view-point that small magma-filled cracks pre-exist at the contact between the chamber and the bedrock [e.g., *Lister and Kerr*, 1991; *McLeod and Tait*, 1999] (see review by *Rubin* [1995]), assumes that failure initiates as soon as the internal pressure reaches a value of the order of the bedrocks' tensile strength [e.g., *Tait et al.*, 1989; *Gudmundsson et al.*, 2002; *Gudmundsson*, 2006; *Pinel and Jaupart*, 2005]. The other view considers that such pre-existing magma-filled cracks are not significant (for example, they freeze before being able to propagate), and in this case bedrock failure at the chamber's wall becomes dependent on the gravity body force [e.g., *Sammis and Julian*, 1987; *Grosfils*, 2007]. In section 2 we briefly review previous studies, emphasizing the latter approach which is the one that we develop here. We recall how *Grosfils* [2007] argued that for tensile failure to occur at a chamber's wall, the hoop stress must account for the lithostatic stress component, thus leading to a critical overpressure an order of magnitude greater than the tensile strength. *Gerbault* [2012] showed with two-dimensional (2D) analytical and numerical models that when accounting for gravity and a depth-dependent failure criterion, failure initiates in mode II at the chamber wall instead of in mode I.

[4] Section 3 of our study completes *Gerbault*'s [2012] study with more detailed numerical benchmarks of the surface displacements and patterns of localized deformation produced around an infinitely long inflating cylinder. We show when departure from elastic solutions occur, i.e., when the plasticized (i.e., fractured) domain connects the chamber and the ground surface. Because the problem is formulated in a way very similar to studies seeking for the critical support pressures around tunnels, we also display a case of internal deflation. The results are compared with standard fault pattern predictions from tunneling engineering [*d'Escatha and Mandel*, 1974]. In section 4, we employ hydromechanical simulations to analyze the effect of fluid pressure in pores on the initiation of shear failure. We demonstrate the sensitivity of failure to initial bedrock porosity. Acknowledging the limitations of our theoretical approach to real processes, we conclude with a discussion of the possible contexts for either tensile or shear failure initiating around magmatic chambers and on the perspectives to improve our understanding of this process in nature.

2. Analytical Solutions of Displacements Produced by Internal Overpressure

[5] In the quest for determining the state of internal pressure that triggers the onset and propagation of failure around an overpressurized magmatic source, we shall consider the simplest idealized shapes of either spherical (3D) or circular (2D) sources in a homogeneous half-space. These assumptions coincide with those of many previous studies, thus allowing a direct comparison. The relevance of accounting for changes in volume [e.g., *Johnson et al.*, 2000; *Rivalta and Segall*, 2008] instead of a homogeneous internal overpressure is also beyond the scope of this paper. In this brief review, we shall first provide an explicit solution for surface displacements in plane-strain condition. This solution had not been published before (to our knowledge), and it is useful to compare it with the well-known 3D solution from *Mogi* [1958]. After briefly summarizing the existing predictions of tensile failure out of a magmatic chamber, we recall *Gerbault*'s [2012] demonstration of the occurrence of shear failure instead of tensile failure when gravity is accounted for. Finally we cite previous studies which for various practical reasons, have not

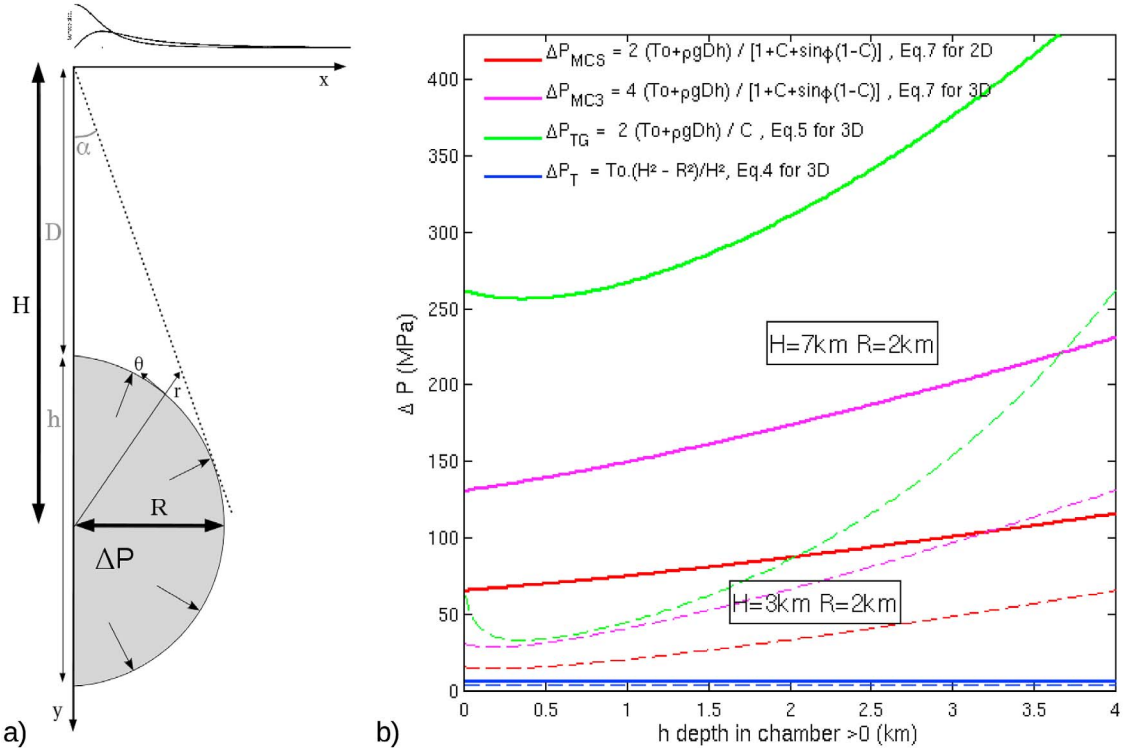

Figure 1. (a) Parametric definition of the problem. Grey values are those used by *Grosfils* [2007]. Top lines are typical shapes of displacements at the surface. (b) Plot of critical overpressure to initiate either tensile or shear failure around a chamber at depth h from its crest (modified from *Gerbault* [2012]).

sought to specify the state of overpressure associated to modeled failure patterns.

2.1. Analytical Expressions of the Hoop Stress and Surface Displacements

[6] When seeking for an analytical solution of the displacements at the surface of an overpressurized magmatic inclusion, *Mogi* [1958] provided a reasonable first order approximation for a deep point source satisfying $H \gg R$ (in 3D). R being the cavity radius and H the depth to its center, μ the bedrock's shear modulus (Poisson's coefficient is equal to 0.25) and x the horizontal coordinate, the solution is

$$U_x = \frac{3 \cdot \Delta P}{4\mu} \cdot \frac{R^3 \cdot x}{(x^2 + H^2)^{3/2}}, \quad U_y = \frac{3 \cdot \Delta P}{4\mu} \cdot \frac{R^3 \cdot H}{(x^2 + H^2)^{3/2}}. \tag{1}$$

This approximation was then developed and generalized to shallow sources by *McTigue* [1987].

[7] In two-dimensions in turn, while the stress field produced by a pressurized circular cavity was solved exactly by *Jeffery* [1921] in bipolar coordinates, not the displacements. The hoop stress at the chamber wall is expressed according to a free surface factor C, expressed either with R and H, or with the angle α between the vertical axis of symmetry and the line joining the surface origin X_o to a point on the chamber wall [*Jeffery*, 1921] (Figure 1a): $C = 1 + 2 \tan^2 \alpha$. As mentioned by *Jeffery* [1921], failure should initiate either at the free surface or at the cavity walls, depending on the shape ratio R/H. It should initiate at the wall where the hoop stress $\sigma_{\theta\theta}$ is maximum, $\sigma_m = -\Delta P \cdot (H^2 + R^2)/(H^2 - R^2)$, corresponding to sin $\alpha_m = R/H$. These stress solutions are still applied today to a variety of magmatic sources that present an elongated shape in one horizontal direction [e.g., *Gudmundsson*, 1988, 2006; *Pinel and Jaupart*, 2003, 2005; *Gray and Monaghan*, 2004].

[8] In two-dimensions, the exact analytical solutions of the surface displacements appear not to have been published, and therefore we display them here. They are obtained here from the general expressions derived by *Verruijt* [1998], who used complex variables with a conformal mapping onto a circular ring. Variable α is defined by $R/H = 2\alpha/(1 + \alpha^2)$, and the coordinate system is referred

by $z = x + iy$. Additional variables are defined: $\gamma = (1 - \alpha^2)/(1 + \alpha^2)$, and ζ such that $z = -i \cdot H \cdot \gamma^2 \cdot (1 + \zeta)/(1 - \zeta)$. The displacements at the surface y = 0 are expressed in terms of a stress function $\varphi(z)$ of z: $U_x + iU_y = 2/\mu \cdot (1 - \nu) \cdot \varphi(z)$.

[9] *Verruijt* [1998] provided the function corresponding to a uniform radial stress P acting on a cavity boundary of radius R and depth H: $\Phi(z) = 2i \cdot \Delta P \cdot [-(1 + \alpha^2) + \zeta + \alpha^2/\zeta]$.

[10] The vertical and horizontal displacements are thus deduced (for an infinitely long cylinder):

$$U_x = \frac{\Re(\Phi)}{2\mu} = \frac{3\cdot\Delta P}{4\mu}\cdot\frac{H\cdot(x^2+H^2)}{x^2+\gamma^2\cdot H^2},$$
$$U_y = \frac{\Im(\Phi)}{2\mu} = \frac{3\cdot\Delta P}{2\mu}\cdot\frac{x\cdot H\cdot(x^2+H^2)}{x^2+\gamma^2\cdot H^2}. \quad (2)$$

In section 3.3 analytical and numerical solutions of equations (1) and (2) are compared, illustrating the significant different magnitudes that result from either a two-dimensional (infinitely long) or a three dimensional spherical chamber.

2.2. Predictions of Critical Internal Overpressure to Initiate Tensile Failure

[11] Many authors assume that the same tensile failure criterion applies to the Earth's surface and the chamber walls, that is when the deviatoric stress ($\sigma_{//} = (\sigma_1 - \sigma_3)/2$) exceeds the rocks tensile strength, T [e.g., *Tait et al.*, 1989; *Pinel and Jaupart*, 2003, 2005; *Gudmundsson*, 1988; *Gudmundsson et al.*, 1997]. With this criterion: at the surface, failure is predicted to occur when the internal overpressure reaches the critical value

$$\Delta P_s = T\cdot(H^2 - R^2)/(2R^2), \quad (3)$$

and at the chamber wall, tensile failure is predicted to occur for the critical internal overpressure

$$\Delta P_T = T\cdot(H^2 - R^2)/H^2. \quad (4)$$

This last assumption is justified by the point of view that failure originates from the opening of small pre-existing cracks filled with overpressurized magma at the walls of the reservoir [e.g., *Lister and Kerr*, 1991; *Rubin*, 1993, 1995; *McLeod and Tait*, 1999; *Fialko et al.*, 2001]. The tensile failure condition of equation (4) results from the balance between the internal pressure (let us take the simplest case, $\Delta P - \rho gy$) and the external stress (most simply $\sigma_3 = -\rho gy$) acting normal to the crack's wall, and requiring to attain the bedrock's tensile strength, T. Thus, predicted values of the magmatic internal overpressure ΔP_T are bounded by T, typically ranging between ~6 MPa [*Gudmundsson et al.*, 2002] and 20 MPa [*Pinel and Jaupart*, 2003].

[12] However, for the above condition to be valid, adequate physical conditions must be satisfied at the chamber wall, including that magmatic overpressure (ΔP) is appropriately distributed within a sufficiently large pre-opened crack oriented perpendicular to the chamber wall [e.g., *Sammis and Julian*, 1987]. Critical conditions on local geometries, input pressures and thermally dependent rheologies must be satisfied so that neither does the magmatic source consume the incipient dike, nor does the dike freeze [e.g., *Rubin*, 1993, 1995; *Karlstrom et al.*, 2010, and references therein].

[13] When one starts to consider a situation in which pre-existing incipient dikes may freeze before propagating over significant distances, the stress balance at the chamber wall must rather be written over an elementary volume of bedrock in which a new fracture will nucleate. Along this line of reasoning, *Grosfils* [2007] demonstrated that in order to evaluate the conditions for tensile failure in the bedrock adjacent to the walls of a spherical chamber, gravity must be accounted for in the stress balance. In his reasoning, *Grosfils* [2007] argued that on an elementary volume across the chambers wall, tensile failure should occur when the normal stress, which is the hoop stress $\sigma_{\theta\theta}$, exceeds not only the tensile strength of rocks (T), but also the wall-parallel component of the lithostatic stress (of the form $-\rho gy$ for negative depth y). His expression of the overpressure ΔP_{TG} associated to wall failure then becomes

$$\Delta P_{TG} = 2/C\cdot(T - \rho gy), \quad (5)$$

with C the free surface factor as defined above by *Jeffery* [1921]. This prediction of minimum overpressure ΔP_{TG} for bedrock wall failure produces values about 2 times greater than the lithostatic stress [*Grosfils*, 2007], and contrasts with the classical prediction given in equation (4), stating that failure is bounded by $T < 20$ MPa (Figure 1b).

2.3. Conditions for Shear Failure When Accounting for Gravity

[14] In continuation of the previous line of reasoning, in which the bedrock adjacent to the magmatic chamber remains preserved and sufficiently intact, we recall here how shear failure would rather occur prior to tensile failure [*Gerbault*, 2012]. The

Coulomb criterion of failure relating the tangential and normal stresses via the bedrock friction angle φ and cohesion S_o, can be written in terms of the mean stress ($P = (\sigma_1 + \sigma_3)/2$) and the deviatoric shear stress ($\sigma_{//} = (\sigma_1 - \sigma_3)/2$):

$$\tau_s = S_o - \tan\varphi \cdot \sigma_n, \quad \tau_s = \sigma_{//}\cos\varphi, \quad \sigma_n = -P + \sigma_{//}\sin\varphi. \tag{6}$$

Without gravity, the minimum and maximum principal stress components at the chamber's wall are of opposite sign ($\sigma_1 = -\sigma_3$), so that $P = 0$. The second invariant of the stress field differs for an infinitely long chamber (plane-strain or 2D) and a spherical chamber (axisymmetry or 3D) with either $\sigma_{//} = \Delta P_{MC}$ in the former case, and $\sigma_{//} = \Delta P_{MC}/2$ in the latter case [*Timoshenko and Goodier*, 1970].

[15] When adding gravity, the pressure at the chamber wall may be assumed to coincide with that of the medium at gravitational equilibirum, so that $P = -\rho g y$ (at negative depth y). This value and the free-surface condition $\sigma_1 = -C \cdot \sigma_3$ [e.g., *Gudmundsson*, 1988] are inserted into equation (6). When defining $T_o = S_o/\tan\varphi$, the critical overpressure required for shear failure is obtained. For an infinitely long chamber [*Gerbault*, 2012]

$$\Delta P_{MCS} = 2\sin\varphi \cdot \frac{-\rho g y + T_o}{1 + \sin\varphi + C\cdot(1 - \sin\varphi)}. \tag{7}$$

For a spherical chamber (in 3D), this critical overpressure is basically multiplied by a factor 2. For any given values of H and R, comparison of equations (4), (5) and (7) show that the critical overpressure for shear failure is smaller than that for tensile failure when gravity is accounted for (details in the work of *Gerbault* [2012] (Figure 1b)). In other words, the bedrock adjacent to an inflating magmatic chamber is predicted to yield by shear failure (mode II) rather than by tensile failure (mode I).

2.4. Overpressure in Other Modeling Studies

[16] For the "dike-propagation-from-a-pre-existing-magma-filled-crack" condition to be valid, adequate physical conditions must be satisfied at the chamber wall, including that magmatic overpressure is appropriately distributed within a pre-opened thin crack oriented perpendicular to the chamber wall [e.g., *Sammis and Julian*, 1987]. Critical conditions on local geometries, input pressures and thermally dependent rheologies must be satisfied so that neither does the magmatic source consume the incipient dike, nor does the dike freeze [e.g., *Rubin*, 1993, 1995; *Karlstrom et al.*, 2010, and references therein]. *Dieterich and Decker* [1975] examined the effect of source geometries such as point sources, spheres, circular sills and pill-shapes on surface displacements. The fact that variable geometries of magmatic sources are used in specific field studies indicates that the initial appropriate conditions for dike propagation are not always easily achieved. Thus we believe that the standard approach that consists in using equation (2) cannot be systematically used as a condition for failure around magmatic chambers.

[17] Considering now the other view-point of failure nucleation adjacent to a circular (or spherical) magmatic chamber, very few of the many analog and numerical models have actually addressed quantitatively the link between the state of internal overpressure and the failure (plasticized) domain. There are several methodological reasons to this. First, analog models have difficulties in dealing with the quantification of stresses (e.g., *Roche and Druitt* [2001]; see reviews by *Acocella* [2007] and *Marti et al.* [2008]). Then, numerical models accounting for elasticity (or visco-elasticity) alone, assume a priori that failure occurs at locations where the rocks tensile strength is exceeded and exclude self-consistent plasticity [e.g., *Sartoris et al.*, 1990; *Gudmundsson*, 1988, 2006; *Gudmundsson et al.*, 1997, 2002; *Pinel and Jaupart*, 2005; *Masterlark*, 2007; *Bonafede and Ferrari*, 2009]. Therefore these models cannot address when exactly failure initiates with respect to the level of internal magmatic overpressure. Other models that incorporate self-consistent elasto-plasticity, apply a dilational deformation instead of an internal overpressure [*Chéry et al.*, 1991; *Kusumoto and Takemura*, 2003; *Hardy*, 2008]. Among those that have quantified internal overpressures:

[18] 1. *Chéry et al.* [1991] measured in their elasto-visco-plastic numerical models an overpressure of 30 to 60 MPa, in a chamber located at 10 km depth and for a state of hydrostatic pore fluid pressure in the bedrock. Whereas brittle shear deformation was shown to develop around the chamber, the relatively poor resolution of these models could not reproduce precise patterns of failure.

[19] 2. Models of magmatic chambers with sharp edges produce failure more easily than with an ideal circular shape. For example, *Burov and Guillou-Frottier* [1999] and *Guillou-Frottier et al.* [2000] modeled a cycle of inflation and collapse with only 10 MPa of overpressure in a middle-crust rectangular chamber and with visco-elasto-plastic

rheology. In these 2D models, shear bands link the sharp edges of the chamber and the surface.

[20] 3. *Trasatti et al.* [2005] tested a number of parameters to model surface uplift at Campi Flegrei volcano. Whereas Mogi-type elastic models excluding gravity reproduced the measured uplift for an internal overpressure of at least 80 MPa (equal to the lithostatic pressure at the chamber's crest $D \sim 3200$ m, considered as unrealistic), elasto-plastic models including gravity and a Von Mises failure threshold set to 15 MPa (no depth dependency), reproduced the uplift for an internal overpressure of 45–50 MPa. This study illustrates how greater surface uplift is obtained when accounting for gravity and shear failure, and yet for an overpressure greater than the tensile strength (note that this overpressure fits our equation (7) at the crest, with $\sin(30) \cdot (\rho g D + T) \sim 48$ MPa). Unfortunately *Trasatti et al.* [2005] did not comment much on their choice of a Von Mises yield, neither did they display the geometrical pattern of bedrock failure.

[21] 4. *Gray and Monaghan* [2004] studied how faulting initiated and propagated from the chamber to the surface or the other way down, with a 2D smooth particle method. Whereas these authors prescribe failure according to a Von Mises threshold involving an elegant criterion for damage, neither the distribution of stresses nor the full amount of internal overpressure associated to the modeled failure patterns are provided.

[22] 5. Let us also cite approaches which, while concentrating on the important visco-elastic processes occurring at a chambers wall, assume empirically a Von Mises yield criterion, with overpressure values reaching 50–75 MPa [e.g., *Jellinek and De Paolo*, 2003; *Karlstrom et al.*, 2010].

[23] To date, we find that a gap still remains in the explicit quantification of the state of internal overpressure associated to the propagation of faulting around a chamber. The present paper aims at clarifying this link with the help of numerical models that handle self-consistent elasto-plasticity.

[24] It is useful to mention from engineering mechanics, the classical problem of estimating the critical support pressure of a tunnel. This problem is very similar to our present description of an inflating magmatic chamber, with only a sign difference accounting for underpressure instead of overpressure. With theoretical plasticity, *Caquot and Kerisel* [1956] had provided closed-form solutions of a statical admissible stress field for an upper bound of the support pressure in a frictional and cohesive material. Using the slip-line characteristics method, *d'Escatha and Mandel* [1974] constructed the geometrical pattern of failure, also accounting for gravity and a frictional material. In the following numerical study, we will be displaying a model example with an applied internal underpressure, and in which shear bands develop comparable to the *d'Escatha and Mandel* [1974] solution.

[25] More recently, *Massinas and Sakellariou* [2009] investigated the shape of the plasticized domain around a tunnel using elasto-plastic analytical and numerical models. Their analytical solution is actually equivalent to our solution given in equation (7) (details in the work of *Gerbault* [2012]), and while the geometry of their modeled plasticized domain is comparable to ours, their mesh resolution is once again not sufficient to display precise shear band geometries.

3. Numerical Assumptions and Comparison of Elastic Solutions

[26] The models presented below aim at (1) specifying pressure conditions for the development of either tensile or shear failure around an idealistic infinitely long magmatic chamber (2D approximation similar to the approach taken by *Gudmundsson* [1988], *Pinel and Jaupart* [2003, 2005], and others), and (2) comparing these failure patterns with three numerical codes at given internal overpressure. A three-dimensional approach would have been useful as well, however computational time explodes (several months) as soon as one aims at reproducing detailed localized structures similar in quality to those that are shown below in 2D. Also, for sake of simplicity we do not consider heterogeneities in the bedrock nor elliptical magmatic chambers, which lead to a variety of combinations that are best targeted when a specific case is considered.

3.1. Description of the Numerical Methods

[27] Three numerical codes are used to simulate elasto-plastic deformation resulting from an increase in uniform internal pressure, in order to gain confidence on the quality of the results. With these approaches we shall address the sensitivity of failure initiation to physical and numerical parameters, namely the initial pressure conditions, the mesh geometry, and the hydromechanical coupling

between fluid flow and deformation. The first code used is Parovoz [*Poliakov and Podladchikov*, 1992] and is based on the FLAC finite difference method [*Cundall and Board*, 1988; *Cundall*, 1989]. Parovoz has been adapted and applied to many geodynamical applications at crustal and lithospheric scales [*Podladchikov et al.*, 1993; *Poliakov et al.*, 1993; *Gerbault et al.*, 1998; *Lavier et al.*, 2000; *Burov et al.*, 2003]. The second code is FLAC^{3D} [*Itasca Consulting Group*, 2006], which was designed to simulate geomechanical problems. FLAC^{3D} builds radial meshes and incorporates the coupling between fluid flow and deformation, either in static and dynamic modes [*Itasca Consulting Group*, 2006]. The third code is Adeli [*Hassani et al.*, 1997; *Chéry et al.*, 2001], a finite element method based on the dynamical relaxation method which is also commonly used in a variety of geodynamical problems.

[28] We precise that in this study, the term plasticity refers to a process of failure and fracturing in accordance with the engineering mechanics meaning, rather than with the geological meaning, which usually involves viscous behavior.

3.2. Setup of the Models

[29] The problem is modeled in plane-strain, and assumes that the chamber has a radius $R = 2$ km and is located at $H = 7$ km depth. These values were chosen arbitrarily as an average from reported estimates. For instance, *Mogi* [1958] considered depths greater than 10 km and radii greater than 3 km, *Rivalta and Segall* [2008] studied radii ranging from 0.5 to 4 km and depths from 4 to 10 km, *Battaglia et al.* [2003] tested for the Long Valley caldera radii ranging from 0.5 to 4 km and concluded to a depth of 5.9–7.5 km, and *Kumagai et al.* [2011] determined a depth of 6 km for the source of the Tungurahua volcano in Ecuador. The vertical axis of symmetry passing through the center of the chamber is represented by the left border of the model at $X = 0$. Domain dimensions are 100 km in length and 80 km in depth. Whereas the homogeneity of a medium over such an extent is clearly not realistic on Earth, we are simply respecting here a conventional rule for resolving mechanical problems, consisting in eliminating border effects.

[30] In Parovoz, the mesh is initially defined with square elements of length 25 m, over the first 12 km of the domain. Grid resolution progressively reduces in both directions to approximately 1 km at the bottom right corner of the domain. The total number of mesh elements is 275,000 (meshes are displayed in Appendix A). In order to achieve high mesh resolution with the quadrilaterals of this mesh, we had to mesh the chamber as part of the model domain, and give it elastic properties. To justify this assumption, many studies point to the important proportion of volatile phases in a magmatic chamber, which reduce both its elastic rigidity and its incompressibility [*Bower and Woods*, 1997; *Huppert and Woods*, 2002; *Rivalta and Segall*, 2008]. Thus, the higher the internal Young's modulus at given Poisson's ratio, the more the chamber dilates and «absorbs» its internal pressure, thus transferring less pressure to the outer model domain. Our models built with Parovoz, assume Lamé parameters equal to 1/10th of those outside the chamber (corresponding to $\nu = 0.25$, $E = 5$ GPa, whereas $E = 50$ GPa in the bedrock, an average value for the crust). In this case, modeled stress and deformation become undistinguishable for models with $\nu = 0.25$ and $\nu = 0.45$. The models presented below will show how the presence of an elastic chamber in the model little affects the results, when compared to those produced by Adeli and FLAC^{3D} in which the chamber is excluded. In Adeli the mesh is built with triangles, and in FLAC^{3D}, it is built with quadrilaterals expanding radially from the chamber (see Appendix A). Both meshes are coarser with a minimal elementary size of about 50 m.

[31] In the models, all borders have free-slip boundary conditions, except the ground surface which is free. Along the far field lateral border ($X = 100$ km), such a free-slip condition (zero horizontal displacements) was found to produce less border effects than a fixed boundary condition (zero displacements in both directions). This is explained by the fact that at $X = 100$ km, analytical surface displacements remain significantly different from the zero-value predicted at infinite distance. Rock density is uniform, with $\rho = 2500$ kg/m^3 (an arbitrary value chosen similar to that of *Cayol and Cornet* [1998], for Piton de la Fournaise). The model is initially set with isotropic lithostatic components (weight of overburden rocks), so that a strain of only 1‰ develops as readjustment to the plane-strain conditions [e.g., *Turcotte and Schubert*, 1982].

[32] Conventional Mohr-Coulomb parameters are specified with a friction angle $\varphi = 30°$ and a cohesion $S_o = 10$ MPa (corresponding to a tensile strength $T_o = S_o/\tan\varphi = 17$ MPa), for all three codes, Parovoz, Adeli and FLAC^{3D}. We will also be showing the effect of a cutoff value of the tensile

Table 1. Main Parameters Used in This Study and Value Given for the Reference Model Only

Symbol	Description	Value
R	Radius of chamber	2 km
H	Depth to center of chamber	3, 7 km
D	Depth to crest of chamber [*Grosfils*, 2007], $D = H - R$	
h	Depth inside the chamber, starting from its crest, $h = D - y$	
G	Shear modulus: chamber (for Parovoz models), bedrock	2, 20 GPa
N	Poisson's ratio	0.25
ρ	Density	2500 kg/m^3
g	Gravity	9.81 m^2/s
α	Angle intersecting at the surface origin a wall-point and the vertical axis $x = 0$ [*Jeffery*, 1921]	
C	Free surface factor: $1 + 2 \tan \alpha^2$	
Θ	Angle intersecting at the chamber center a wall-point and the horizontal axis $y = -H$ [*Grosfils*, 2007]	
σ_{xx}	Horizontal stress	
$\sigma_{\theta\theta}$	Hoop stress at the chamber wall	
ΔP	Internal overpressure	
U_x, U_y	Horizontal and vertical displacements at the surface	
P, σ_{II}	Mean stress and deviatoric shear tress	
τ, σ_n	Tangential and normal stress in Coulomb criterion	
φ, S_o	Bedrock friction angle and cohesion in Coulomb criterion	30°, 10 MPa
T, T_o	Bedrock tensile strength, cutoff deduced from S_o	5, 17.3 MPa
ΔP_S, ΔP_T	Critical overpressure for tensile failure at surface and wall	Equation (4)
ΔP_{TG}	Critical overpressure for tensile failure [*Grosfils*, 2007]	Equation (5)
ΔP_{MCS}	Critical overpressure for shear failure [*Gerbault*, 2012]	Equation (7)
λ	Pore pressure ratio that defines pore pressure $p_f = -\lambda \rho g y$	0, 1
n_o	Bedrock initial porosity (for FLAC^{3D} models)	0.01, 0.1

rock strength, T = 5 MPa. Parameter names and values are given in Table 1.

[33] In the numerical models, the application of a pressure which sets elements in a state of stress which exceeds their yield value is not trivial. The internal overpressure (ΔP) is applied in incremental steps ∂p proportional to the numerical time step ∂t, and is inversely proportional to the numerical sound speed (which is defined with the mesh size, density and Lamé parameters [e.g., *Cundall and Board*, 1988]). ∂p is thus set so that the pressure increases fast enough for the total computing time of the run to be reasonable, and slow enough so that deformation resulting from ∂p provides a quasi-static solution.

[34] In the real world, the onset of an eruption or a dike injection acts to liberate confined magmatic fluids from the chamber, and therefore prevents further increase in internal overpressure. However, it may not always be the case; *Wegler et al.* [2006] interpreted continuously increasing shear wave velocities below the Merapi volcano as an indicator of increasing magmatic pressure in between two consecutive eruptions in 1998. The application of an elevated internal overpressure in our models should therefore be associated to the rapid arrival of overpressurized magma which has no time to equilibrate neither thermally nor mechanically with the surrounding bedrock.

3.3. Elastic Solutions (M0)

[35] We first illustrate how analytical solutions of surface displacements differ significantly whether axisymmetric (Mogi's solution, equation (1)) or plane-strain (equation (2)) conditions are assumed. For the conditions of a reference model (R = 2 km, H = 7 km, ΔP = 50 MPa), vertical and horizontal displacements in plane-strain achieve 2.3 m and 1.1 m, whereas in an axisymmetric chamber, they achieve 0.3 m and 0.1 m, respectively. An infinitely long tunnel produces nearly 10 times more deformation than a sphere (Figure 2a).

[36] FEM tests in plane-strain and accounting for only elastic behavior show how surface displacements are very sensitive to the dimensions of the numerical domain. Figure 2b shows that a right-hand side border set 400 km away produces an error of 1% and 2%, respectively for the vertical and horizontal displacements at the surface. A

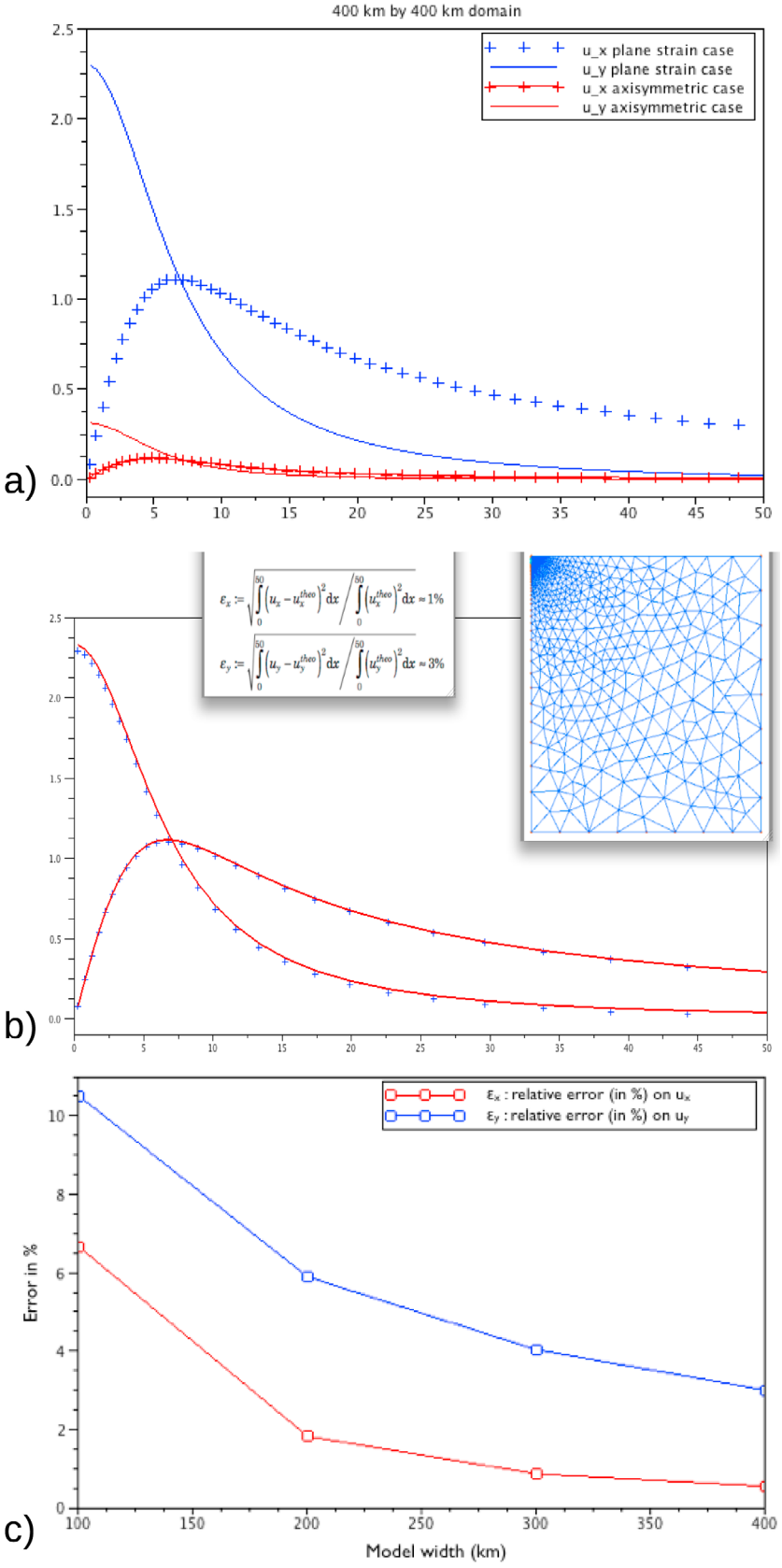
400 km by 400 km domain
u_x plane strain case
u_y plane strain case
u_x axisymmetric case
u_y axisymmetric case
a)
b)
c)
Error in %
Model width (km)
εx : relative error (in %) on ux
εy : relative error (in %) on uy

Figure 2

vertical border set 100 km away produces errors of 6% and 10% (Figure 2c).

[37] Since elasto-plastic behavior is rather expensive in terms of computational time, we must limit the dimensions of the model domain as a tradeoff to a high resolution mesh capable to generate failure structures. Therefore when studying elasto-plastic solutions with the three above mentioned numerical methods, Parovoz, Flac^{3D} and Adeli, the model domain was defined with 100 km in width and 80 km in depth. Thus up to 10% error is expected due to these limited dimensions (Figure 2d).

4. Elasto-plastic Models, Neglecting the Effects of Fluid

4.1. Stages of Deformation With Increasing Overpressure

[38] *Gerbault* [2012] presented sequential results of deformation at increasing internal overpressure, identifying three stages:

[39] Stage 1 corresponds to tensile failure occurring first at $X = 0$, $Y = 0$ at the surface origin, when the applied internal overpressure reaches the predicted value of equation (1), $\Delta P \sim 28$ MPa (numerical time step sampling does not necessarily correspond to exact analytical predictions).

[40] Stage 2 corresponds to shear failure initiating around the chamber, at a ΔP consistent with prediction from equation (7): $\Delta P_{MC} = (-\rho g y + T_o) \cdot \sin\varphi \sim 71$ MPa. With increasing pressure, shear-bands propagate from the chamber wall with an eccentric logarithmic geometry (according to *Nadai* [1950]). They have an angle of 60° one from the other and form outward dipping reverse faults, consistent with non-associated plasticity predictions [e.g., *d'Escatha and Mandel*, 1974; *Vermeer and de Borst*, 1984; *Gerbault et al.*, 1998].

[41] Stage 3 begins when the two plasticized domains, propagating first inward from the ground surface and second, upwards from the chamber walls, become connected. Shear bands continue to expand outwards from the chamber.

[42] In the next sections we will compare solutions produced for each of these three stages.

4.2. Modeled Surface Deformation in Case of a Mostly Elastic Domain (Stage 1, M1)

[43] This series of models (M1) serves as a first benchmark between all three codes Parovoz Adeli and Flac^{3D}. A fixed internal pressure $\Delta P = 50$ MPa is applied (Figure 3). Therefore we are within stage 1, where apart from about a 100 m close to the origin at the top surface, the whole domain remains elastic.

[44] When comparing the results, the computed superficial displacements differ from the analytical solution from 6 to 18% in all three models (U_x = 2.1–2.2 m, Table 2). We consider that these errors are satisfying when recalling that about 10% error is already expected due to border effects alone (see section 3.3).

4.3. Comparison of Models at Well Developed Elasto-plastic Stage 2 (M2)

[45] We apply now an overpressure $\Delta P = 120$ MPa, which corresponds to a state of plastification just before stage 3 (fault connection). The comparison of stress and deformation patterns between different meshes raises the following points (Figure 4):

[46] 1. The model produced by Parovoz produces a zone of failure over a thickness of about 1 km around the chamber, coeval with failure at the surface down to about 2 km depth (Figure 4b).

[47] 2. Model M2′ produced by Adeli displays a similar geometry of failure at a significantly higher level of chamber overpressure equal to 150 MPa instead of 120 MPa (Figure 4c). This is because the failure yield stress is expressed according to a Drucker-Prager criterion instead of a Mohr-Coulomb criterion (and despite a standard adaptation of friction and cohesion parameters). At ΔP = 120 MPa, the radius of the failed domain around the chamber is only 700 m and surface normal faulting extends down to only 1.8 km depth. However, surface displacements at 120 MPa compare well with those produced by Parovoz (Figure 4a).

[48] 3. Model M2″ with Flac^{3D} are loaded instantaneously, and produce an envelope of the plasti-

Figure 2. Elastic solutions for surface displacements (models M0). (a) Analytical solutions for plane strain (2D, equation (2), blue lines) and axisymmetric (3D, equation (1), red lines) cases. (b) Comparison of the numerical elastic solution (blue crosses) with the analytical plane-strain solution (equation (2)), for a horizontal size of the model of 400 km. (c) Errors produced by the numerical solutions for different sizes of the model domain. 10% error in vertical displacement (U_y, in blue) occurs when the model domain is 100 km wide.

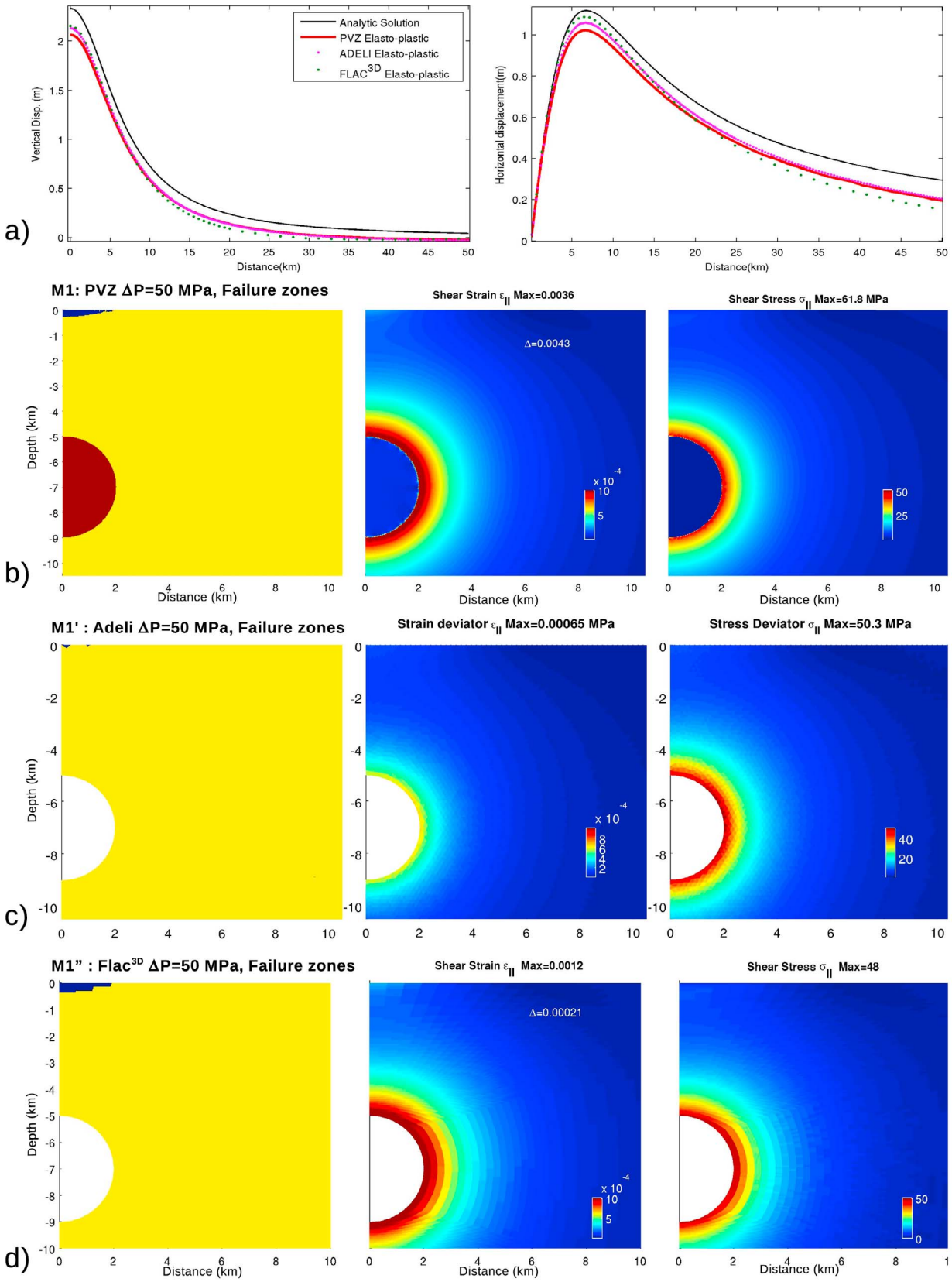

Figure 3. Comparison of models M1 for a field overpressure of ΔP = 50 MPa. (a) Vertical (left) and horizontal (right) surface displacements. (b) M1 is Parovoz, (c) M1′ is Adeli, and (d) M1″ is Flac^{3D}; panels from left to right are the failure zones, the shear strain, and the shear stress.

Table 2. Setup Conditions and Models Results[a]

Model Name	Figure	Code	Gravity Porosity	Tensile Limit, T	ΔP (MPa)	Fail. Stage	Shear Strain, ε_{II}	Surface, Uy (m)	Error, Uy	Error, Ux
M1	3a	Parovoz	G	17.3	50	1	0.004	2.1	0.16	0.13
M1′	3b	ADELI	G	17.3	50	1	0.001	2.13	0.14	0.06
M1″	3c	FLAC^{3D}	G	17.3	50	1	0.001	2.2	0.18	0.16
M2	4a	Parovoz	G	17.3	120	2	0.029	4.9	**0.21**	0.17
M2′	4b	ADELI	G	17.3	120	2	0.029	4.8	0.11	0.04
M2″	4c	FLAC^{3D}	G	17.3	120	2	0.005	5.1	0.19	**0.49**
M3	6a	Parovoz	G	5	148	3	0.134	25	**1.21**	**1.67**
M3′	6b	Parovoz	G	5	65	3	0.022	5	**0.30**	**0.20**
M4	7	Parovoz	G	5	−130	3	0.079	−18	**0.99**	**1.88**
M5	8a	Parovoz	HPP	5	60	2	0.005	2.37	**0.26**	0.16
M5′	8b	FLAC^{3D}	n = 0.01	5	60	2	0.002	2.21	**0.22**	**0.40**
M5″	8c	FLAC^{3D}	n = 0.1	5	60	2	0.002	2.23	**0.33**	**0.38**
M6	9a	Parovoz	LPP	17.3	20	2	0.008	1.9	**0.60**	**0.39**
M6′	9b	ADELI	0	17.3	20	2	0.001	1.2	**0.29**	0.07
M6″	9c	FLAC^{3D}	0	17.3	20	2	0.001	1.3	**0.38**	**0.30**
M7	10a	FLAC^{3D}	n = 0.1	17.3	20	2	0.001	1.4	**0.82**	**0.51**
M7′	10b	FLAC^{3D}	n = 0.01	17.3	20	2	0.002	2.1	**1.21**	**0.59**

[a]The first column displays models names, the second column gives the associated figure, and the third column the numerical code. Column four indicates the gravity and fluid state (G or 0 for gravity or not, LPP for lithostatic pore pressure, and initial porosity n_o for models 7). Columns five and six indicate values in MPa of the tensile strength T and the applied internal overpressure ΔP, respectively. The last columns describe the results, according to their stage of failure: 1 for failure at the surface only, 2 for failure at the walls, and 3 when the plasticized domain is connected. Then the maximum shear strain (ε_{II}) and maximum surface topography U_y are given. The two last columns display errors in surface displacements U_y and U_x, with respect to the theoretical values of equation (2) (10% error is expected already due to the finite dimensions of the model). Bolded numbers are errors >20%.

cized domain which is consistent with the 2 previous models, and similar to previous results by *Chéry et al.* [1991] or *Massinas and Sakellariou* [2009]. Localized shear bands cannot form because of the coarse mesh resolution (Figure 4d).

[49] As the mesh is coarser in different models, shear bands are also coarser: this is a common feature of numerical modeling of plastic (e.g., faulting) behavior. The loss of unicity of the mathematical solution causes shear band geometries to depend on numerical characteristics such as mesh resolution [e.g., *Prevost and Loret*, 1990; *Kaus*, 2010]. The validity of the models in reproducing similar faulting patterns appears limited by the specificities of each modeling approach, e.g., an elastic chamber with Parovoz, a slightly different yield stress formulation with Adeli, and a sudden application of overpressure with Flac^{3D}.

[50] The ground surface displacements differ by about 10% one numerical model with the other (Figure 4 and Table 2), except for model M2″. At this stage, they differ from the elastic solution by slightly lower surface uplift at the origin, and lower surface uplift at distance (around position X = 20 km). Horizontal displacements in turn, exceed the elastic solution at the origin, and they also underestimate it around X = 20 km (M2″ with Flac^{3D} model produces the less good fit).

4.4. Modeled Deformation During Stage 3, Plastic Domain (M3)

[51] Now the modeled elasto-plastic solutions are displayed after Stage 3, which occurs when the plastic domain is connected in between the chamber and the surface (Figures 5 and 6).

[52] Figure 5 shows how maximum vertical displacements start to overshoot significantly the elastic solution, from this stage 3, in all three models. The moment when the crest of the chamber starts to yield occurs at about 70 MPa in the first Parovoz model, consistent with the analytical prediction (equation (7)). Failure produced by the Adeli model is delayed with respect to the two other models, because of the formulation of the yield criterion which renders the bedrock more rigid. The third Flac^{3D} model produces intermediate surface displacements with respect to the two other models.

[53] Figure 6 displays the modeled faulted domain at an advanced stage: most of the deformation localizes along the curved shear bands that connect the edges of the chamber wall to the surface. As deformation continues to localize with pressure increase, these active shear bands will tend to adopt a vertical geometry which reminds of the classical downsag structures described elsewhere in the literature (e.g., *Acocella* [2007], for deflation). This typical failure pattern shows that eventually at large

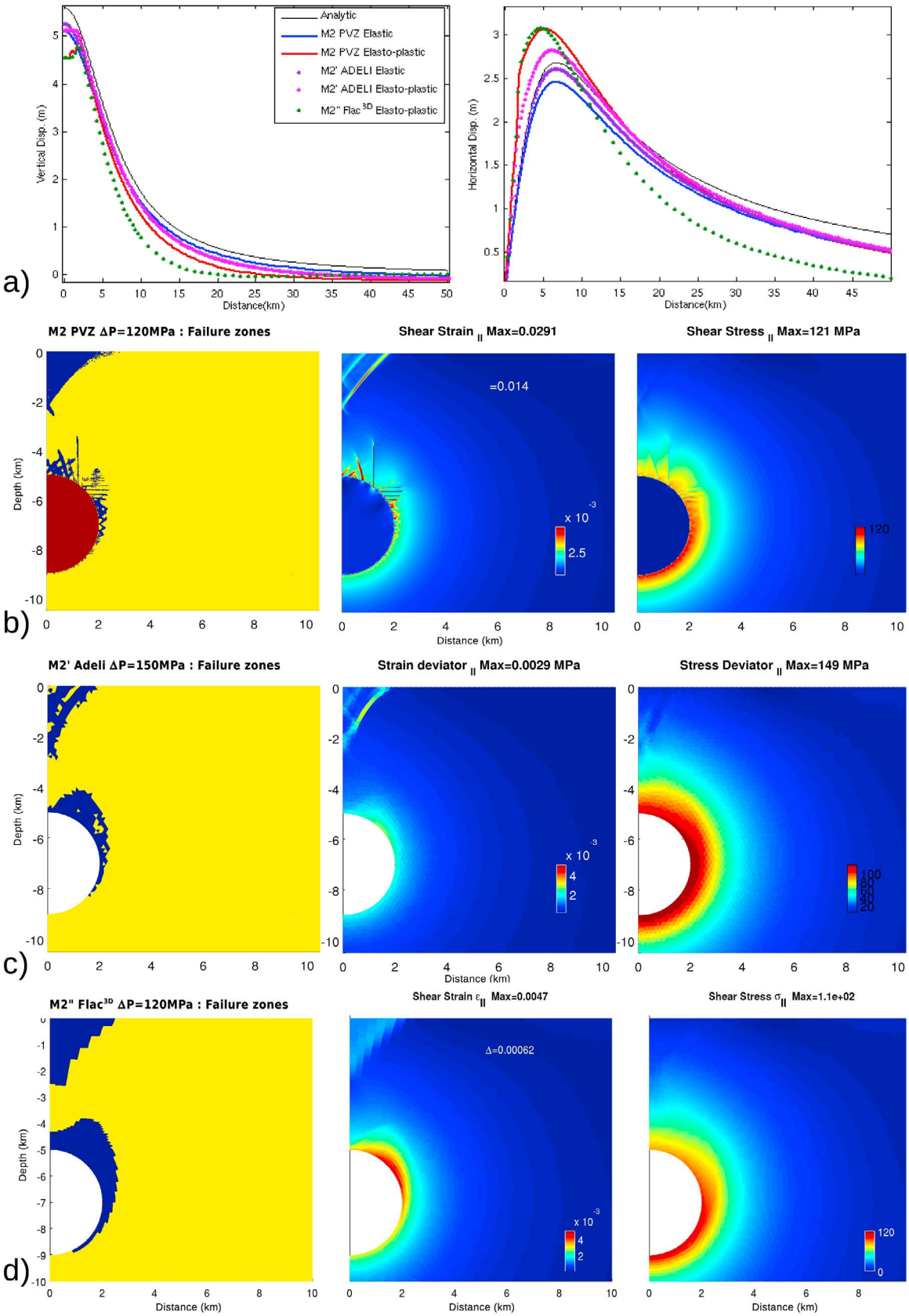
a)
Analytic
M2 PVZ Elastic
M2 PVZ Elasto-plastic
M2' ADELI Elastic
M2' ADELI Elasto-plastic
M2" Flac 3D Elasto-plastic
Vertical Disp. (m)
Horizontal Disp. (m)
Distance(km)
b)
M2 PVZ ΔP=120MPa : Failure zones
Shear Strain II Max=0.0291
Shear Stress II Max=121 MPa
=0.014
x 10-3
2.5
120
Depth (km)
Distance (km)
c)
M2' Adeli ΔP=150MPa : Failure zones
Strain deviator II Max=0.0029 MPa
Stress Deviator II Max=149 MPa
x 10-3
4
2
100
80
60
40
20
d)
M2" Flac3D ΔP=120MPa : Failure zones
Shear Strain εII Max=0.0047
Shear Stress σII Max=1.1e+02
Δ=0.00062
x 10-3
4
2
120
0

Figure 4

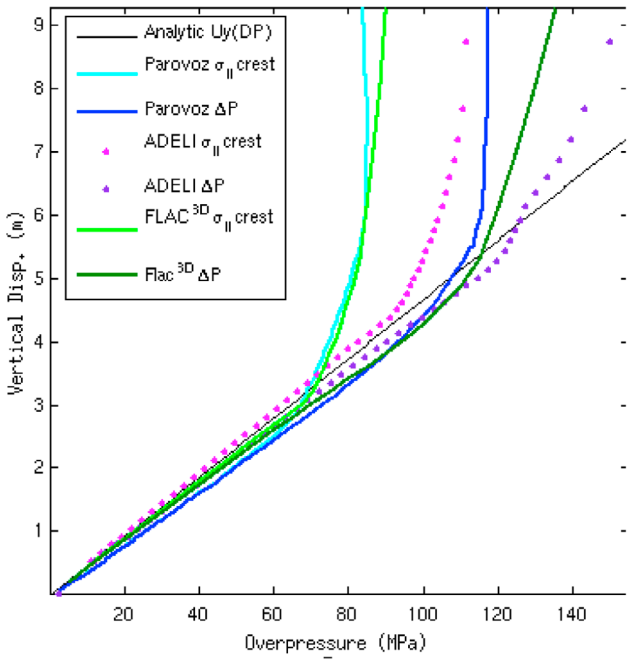

Figure 5. Maximum surface uplift as a function of increasing internal overpressure (models M1, M2 and M3): departure from elastic solutions become significant when the entire domain from the chamber to the surface becomes plastic, when ΔP approaches 100 MPa. Adeli results are delayed due to the slightly different yield criterion. Plots displaying the shear stress at the chamber crest (labeled σ_{II} crest) show that the yield is reached at 70 MPa for Parovoz and Flac^{3D}.

strains, localized deformation responds to the minimization of energy integrated over the entire domain between the chamber and the surface, and not only from the local yield stress distribution [e.g., *Masek and Duncan*, 1998; *Gerbault et al.*, 1998]. In other words, while the initial curved shear bands result from the elastic stress distribution, at large strains, these shear bands tend to straighten vertically, following the shortest distance linking the chamber and the free top surface.

[54] When investigating for which conditions the bedrock around a magmatic chamber would fail in tension, *Gerbault* [2012] showed that with a tensile strength cutoff set to T = 5 MPa, tensile failure develops over the first ~500 m from the ground surface, whereas shear failure still occurs everywhere else as described above and for identical levels of the internal overpressure. It is interesting to look at how the two systems of failure connect at stage 3, for two different shape ratios R/H:

[55] 1. Figure 6a is a model with a geometry similar to that above, i.e., with depth H = 7 km and a radius R = 2 km. Tensile failure (shown in light blue as opposed to dark blue for shear failure in Figure 6a) and vertical shear bands merge at about 500 m depth, over a width equivalent to the chamber's radius R. At the surface, tensile failure occurs over a width of nearly $2R$.

[56] 2. Figure 6b displays the results for a chamber located at H = 3 km depth and of radius R = 2 km. One might have anticipated that the proximity of the chamber to the free surface will enhance the occurrence of tensile failure. But shear failure still originates from the chamber wall, and tensile failure still remains confined to the top first kilometer. A beautiful geometrical pattern appears, in which vertical shear bands initiating from the chamber wall, concentrate at a distance from the crest, and propagate upwards up to about 500 m depth, where they merge with the domain of tensile failure. This geometry suggests that perhaps, fluid material being transferred vertically from the chamber along the shear faults and then intruding at ~500 m depth into zones of horizontal tensile stress, may produce «sills». This depth is controlled by the value of T.

Figure 4. Models M2 at stage 2, for a field overpressure ΔP = 120 MPa. (a) Vertical (left) and horizontal (right) surface displacements. (b) M2 is Parovoz, (c) M2′ is Adeli but for ΔP = 150 MPa, and (d) M2″ is Flac^{3D}; panels from left to right are the failure zones, the shear strain, and the shear stress.

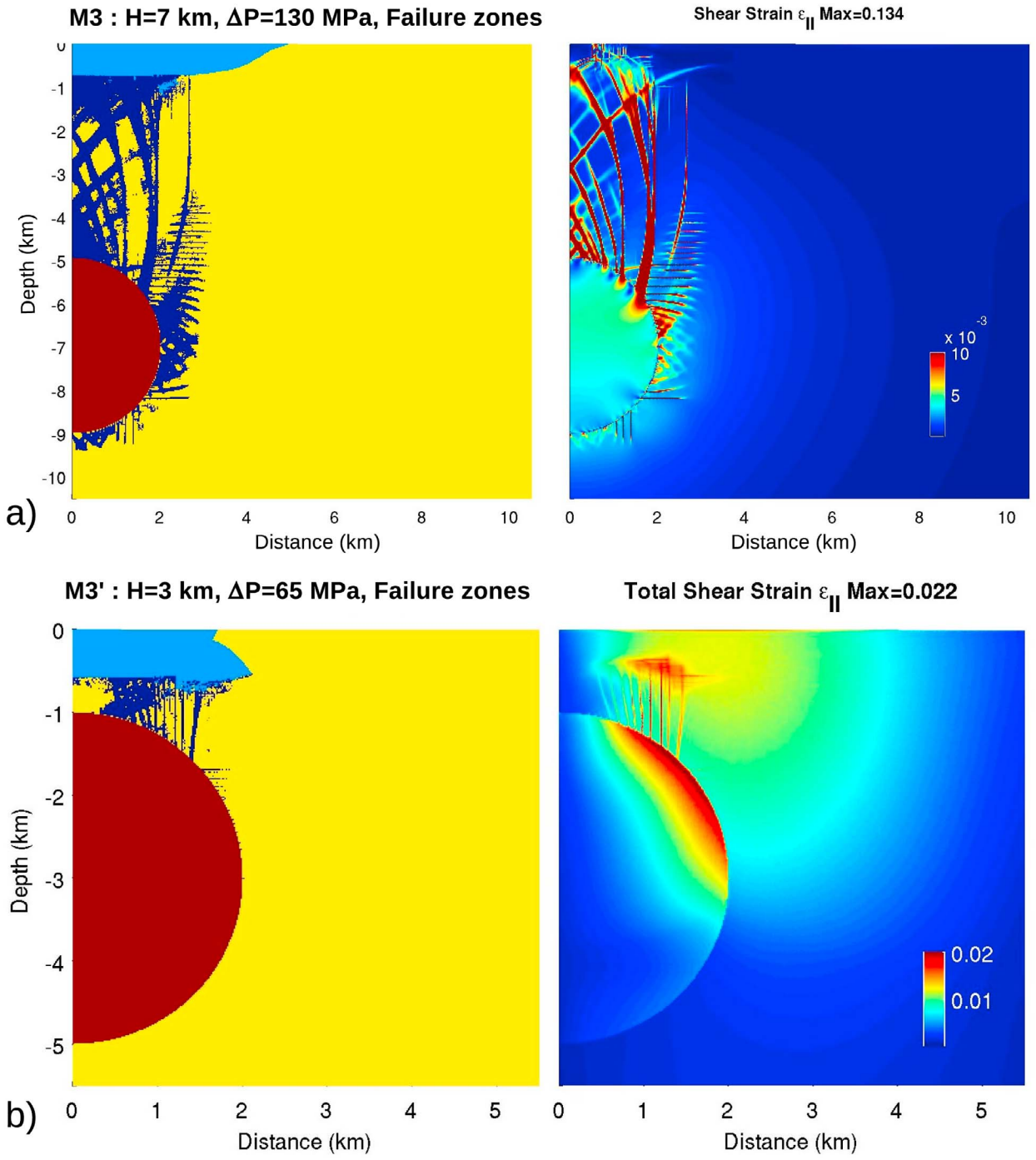

Figure 6. Models M3 at stage 3, proceeded with Parovoz, and with a tensile cutoff $T = 5$ MPa. Light blue zones indicate domains of tensile failure as opposed to dark blue zones indicating shear failure, as in previous figures. Failure domain and shear strain at (a) $\Delta P = 135$ MPa for a chamber $H = 7$ km and $R = 2$ km, and (b) at $\Delta P = 65$ MPa for a chamber $H = 3$ km and $R = 2$ km.

More elaborated hydromechanical modeling is required to confirm this proposition.

[57] One noticeable difference in this model ($R/H = 2/3$) with respect to the previous model (with $R/H = 2/7$), is that shear bands localize in an area closer to the vertical axis of the domain. It depends on the location of maximum deviatoric stress along the walls of the chamber, which directly relates to the free-surface factor C, as has been discussed by

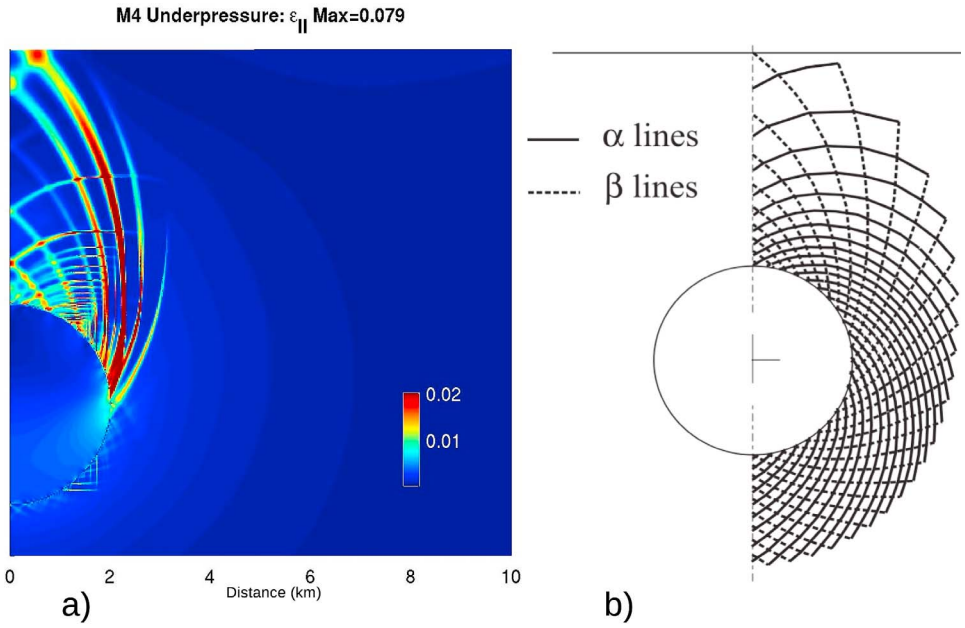

Figure 7. Model M4: (a) underpressure $\Delta P = -130$ MPa for a chamber $H = 7$ km and $R = 2$ km, and a friction $\varphi = 20°$; (b) graphical semi-analytical solution calculated by *d'Escatha and Mandel* [1974].

Grosfils [2007]. We recall that a distinction exists between the location of failure onset at the chamber wall, and the location of subsequent most active shear bands that connect to the surface, which satisfies a pattern of energy minimization [e.g., *Masek and Duncan*, 1998].

4.5. Case of an Applied Underpressure (M4)

[58] In the theory of plasticity used in engineering mechanics, the critical state of stress for failure is assumed to be reached everywhere, and the solution provides the geometry of potential slip-lines along which rigid blocks slide. In elasto-plasticity, this type of solution thus becomes valid once a sufficient portion of the domain has reached its yield stress state [*Gerbault et al.*, 1998]. It is the case here in our study from Stage 3, as opposed to previous Stages 1 and 2 where the elastic solution remains valid because an elastic core remains in between the chamber and the surface.

[59] As mentioned in section 2.4, tunneling engineers have long been studying the critical support pressure of a tunnel, and graphical solutions based on theoretical plasticity have been proposed by *d'Escatha and Mandel* [1974], accounting for gravity and for various angles of bedrock friction. Since both formulations of a deflating tunnel and an inflating chamber are similar, it is useful to compare our numerical solution at stage 3 with their calculation. Therefore we display the model in Figure 7a, which was obtained with the application of an underpressure instead of an overpressure (thus a switch in sign of ΔP), and a friction angle equal to 20° instead of 30°. This simple change in sign of the internal overpressure produces a pattern of eccentric conjugated shear bands, differing from our previous model M3 by a global rotation of 90°, including also a rotation of 90° of the angle from which they depart from the chamber wall (due to the switch in orientation of principal stresses). This solution compares with the eccentric pattern calculated by *d'Escatha and Mandel* [1974] (Figure 7b).

[60] When transposing this case to the field, the relative orientation of conjugate fault systems with respect to the location of the magmatic body (i.e., direction of elongation of block lozenges) serves as an indicator to differentiate inflating-related from deflating-related structures.

5. The Effect of Fluid Pressure on Bedrock Deformation

[61] A process that must play a role in the mode of fracturing around magmatic chambers is the state of pore fluid pressure in the bedrock. Here we intend to illustrate its prime influence, first with a classical one-way coupling approach based on a modification of the effective normal stress in the yield

criterion, and second with a more realistic two-way hydromechanical coupling based on the undrained response of a porous bedrock.

[62] One-way coupling is achieved with Parovoz, in which the yield criterion can account for the effect of a constant fluid pore pressure in the bedrock. The approximation proposed by *Hubbert and Rubey* [1959] is used, which expressed fluid pore pressure p_f in terms of the vertical lithostatic stress and the pore fluid pressure ratio λ, so that $p_f = -\lambda\rho g y$. In a rock of density 2500 kg/m^3, λ = 0.4 for hydrostatic fluid pressures, and λ = 1 for lithostatic pore fluid pressures. The effective normal stress $\sigma_{eff} = \sigma_n - p_f$ is then involved in the Mohr-Coulomb yield criterion so that

$$\tau = S_o - \tan\varphi \cdot (\sigma_n - p_f). \quad (8)$$

While hydrostatic pore fluid pressure is thought to describe appropriately a common state of the crust [*Townend and Zoback*, 2000], lithostatic pore fluid pressure may also exist in nature since many well data indicate values of λ reaching 0.9 [*Engelder and Leftwich*, 1997; *Hillis*, 2003].

[63] Two-way coupling is simulated with the commercial code FLAC^{3D} which allows to account for hydromechanical processes in a porous medium saturated with water in liquid phase. The initial conditions are thus identical to those prescribed in the Parovoz models, but an initial fluid pressure is assumed that follows a constant hydrostatic gradient with depth. Loading at the chamber wall is now applied instantaneously. The associated fluid pressure and deformation response is mainly undrained (i.e., instantaneous response relative to the subsequent flow response), so that the influence of fluid flow and permeability on the results is negligible. Consequently, the change in fluid pressure (Δp_f) varies according to the change in the ratio of volumetric total strain (or dilatation), and thus according to the initial rock porosity (n_0)

$$\Delta p_f = -K_f \cdot \Delta V / V \quad (9)$$

where K_f is the fluid bulk modulus (K_f = 2 GPa), V is the initial pore volume ($V = n_0$ in a unit volume of rock, if the pore spaces are fully saturated with fluid), and ΔV is the volume change due to deformation. Thus, fluid pressure is now driven by localized volume expansion (ΔV positive) or contraction (ΔV negative).

[64] *Gerbault* [2012] showed with the Parovoz code, that when accounting for a hydrostatic pore fluid pressure ratio, shear failure still initiated at the chamber wall, whereas with a lithostatic pore fluid pressure, tensile failure occurred instead. Below, we benchmark these results and test the effects of accounting for either one-way or two-way hydromechanical coupling.

5.1. Hydrostatic Pore Fluid Pressure, One- and Two-Way Coupling (M5)

[65] In this section a series of models M5 explores the effect of an initially hydrostatic pore fluid pressure in the bedrock on failure propagation. These models account for a tensile strength T = 5 MPa, and an internal overpressure arbitrarily set to ΔP = 60 MPa.

[66] A first reference model M5 is displayed Figure 8b, and corresponds to a Parovoz model assuming the one-way hydromechanical coupling described in the previous section. Tensile failure develops only over the first ~500 m below the surface. Shear failure is incipient along the chamber wall, but has initiated at $\Delta P \sim$ 43 MPa (consistent with equations (7) and (8)).

[67] To test the effect of two-way hydromechanical coupling, two additional models M5′ and M5″ are set with Flac^{3D} in which the initial porosity (n_0) is set to 0.01 and 0.1, respectively (this range of porosities corresponds to values used in the works of *Hurwitz et al.* [2007] and *Hutnak et al.* [2009]). The "triangular" domain of tensile failure near the surface is slightly narrower and deeper than that obtained in model M5 with Parovoz, and reaches 1 km depth in model M5′ with the smallest porosity value n_0 = 0.01. Shear failure occurs around the chamber wall over a significantly greater extent than in model M5, reaching a thickness of about 200 m and 500 m for models with high (M5″, n_0 = 0.1) and low porosity (M5′, n_0 = 0.01), respectively (Figures 8c–8d). This larger failure extent is related to a greater volumetric deformation ($\Delta V/V$) when the porosity is low. This induces a greater variation in fluid pressure that reaches a maximum value of Δp_f = 4.3 MPa and 13 MPa, respectively for models M5″ and M5′ (rightmost plots in Figures 8b and 8c).

5.2. Lithostatic Pore Fluid Pressure, One-Way Coupling (M6)

[68] A series of models (M6) consider a lithostatic pore fluid pressure assuming one-way coupling. In the first Parovoz model M6, the pore fluid ratio is set lithostatic in the bedrock (λ = 1, $p_f = -\rho g y$). In this case, and for an overpressure of only ΔP =

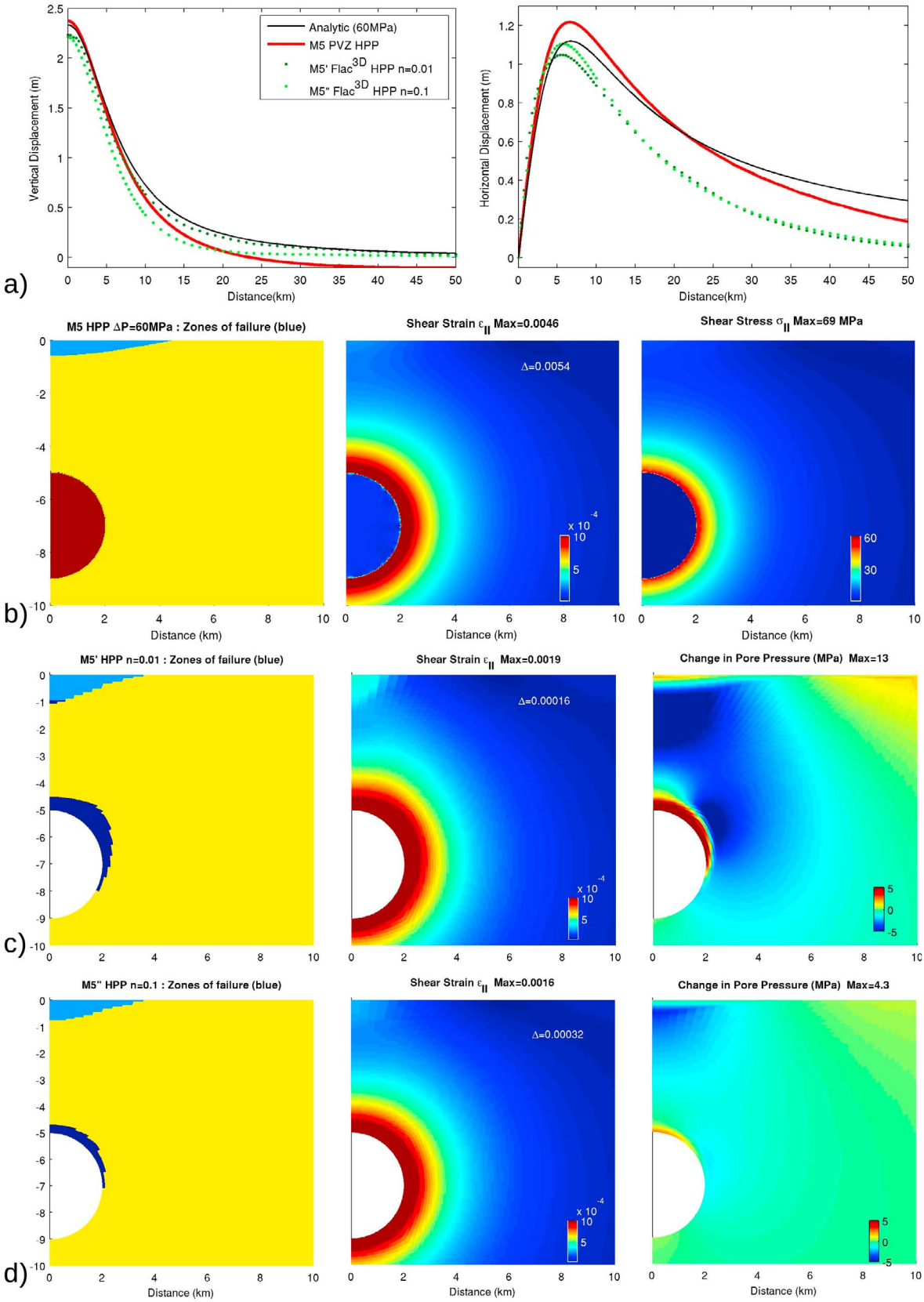
a)
Analytic (60MPa)
M5 PVZ HPP
M5' Flac3D HPP n=0.01
M5" Flac3D HPP n=0.1
Vertical Displacement (m)
Horizontal Displacement (m)
Distance(km)
b)
M5 HPP ΔP=60MPa : Zones of failure (blue)
Shear Strain ε_II Max=0.0046
Δ=0.0054
Shear Stress σ_II Max=69 MPa
c)
M5' HPP n=0.01 : Zones of failure (blue)
Shear Strain ε_II Max=0.0019
Δ=0.00016
Change in Pore Pressure (MPa) Max=13
d)
M5" HPP n=0.1 : Zones of failure (blue)
Shear Strain ε_II Max=0.0016
Δ=0.00032
Change in Pore Pressure (MPa) Max=4.3
Distance (km)

Figure 8

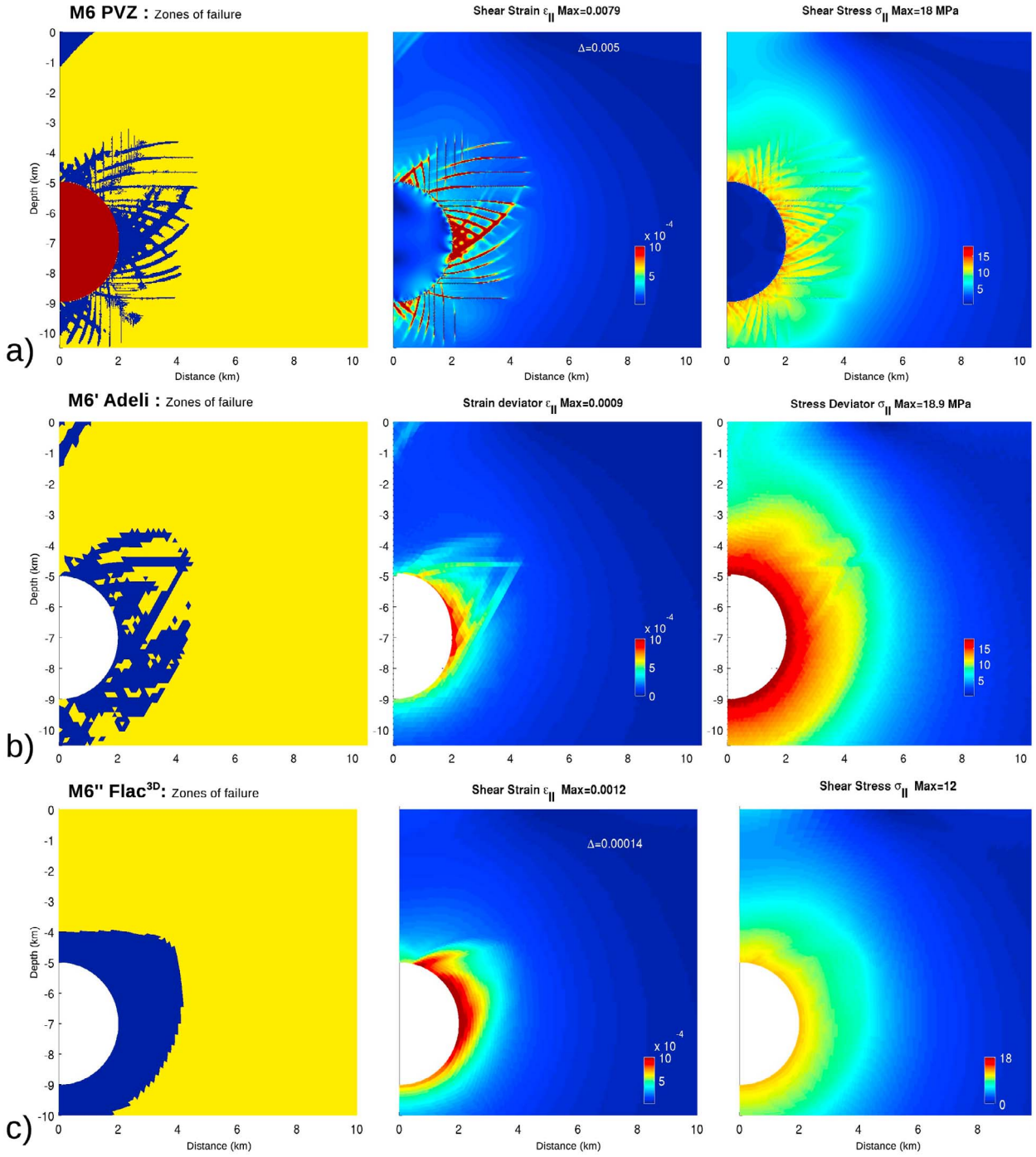

Figure 9. Models M6 with one-way coupling for a lithostatic pore fluid pressure in the bedrock. Solution for internal overpressure $\Delta P = 20$ MPa, with (a) Parovoz and an effective lithostatic pore fluid pressure (LPP) in the yield criterion. Models (b) M6′ with Adeli, and (c) M6″ with Flac^{3D}, both without gravity.

Figure 8. Models M5 predicting failure for a hydrostatic pore fluid pressure (HPP) in the bedrock. Solution for internal overpressure $\Delta P = 60$ MPa, with (a) Parovoz and a one-way coupling using a hydrostatic pore fluid pressure ratio in the yield crierion (M5), and with Flac^{3D} accounting for two-way coupling relating strain changes to fluid-pressure changes, for an initial porosity (b) $n_o = 0.01$ for M5′ (c) and $n_o = 0.1$ for M5″.

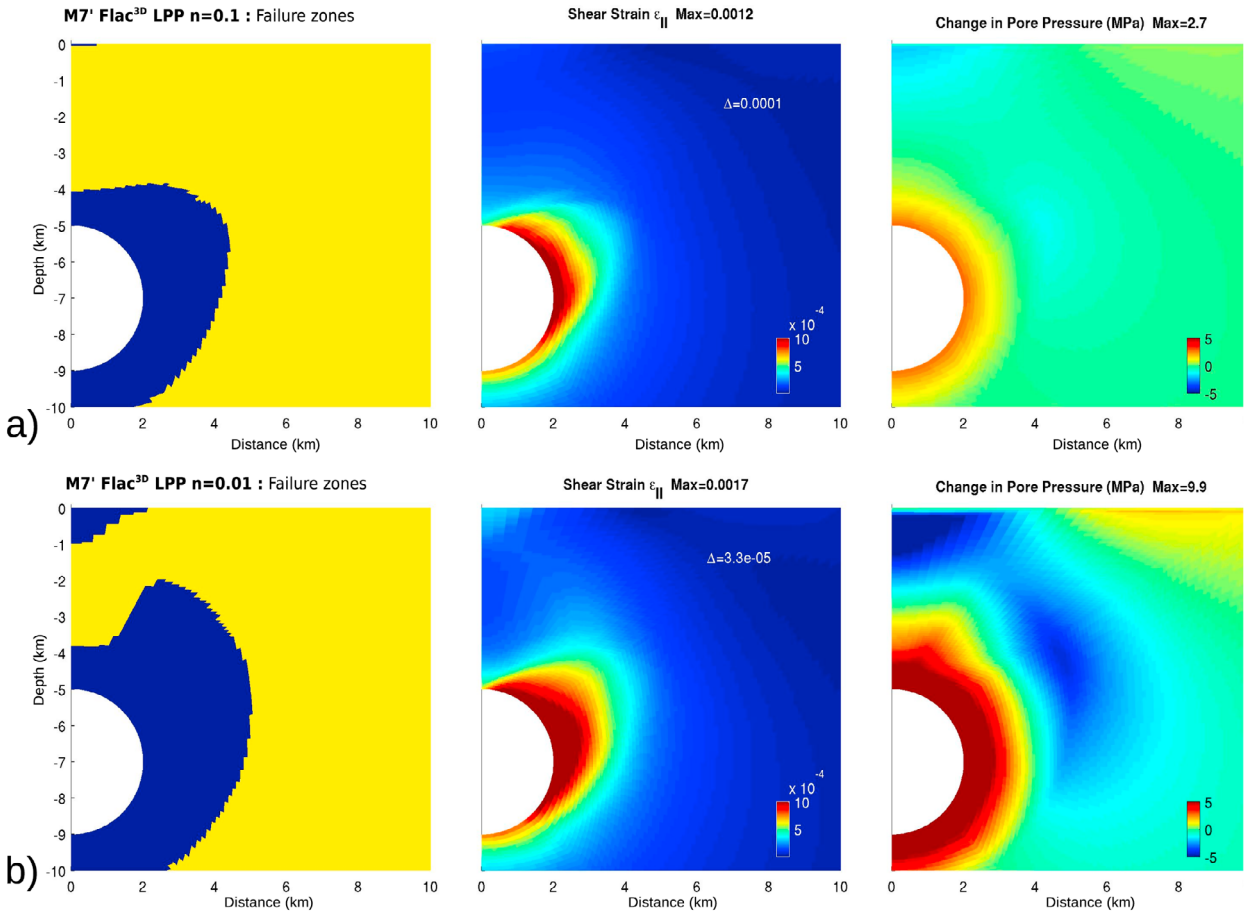

Figure 10. Flac^{3D} models M7 and M7′ showing the effect of two-way coupling at initially lithostatic pore fluid pressure (LPP), for an internal overpressure ΔP = 20 MPa (a) with porosity n_o = 0.1 and (b) with n_o = 0.01. From left to right, failure zones, shear strain, shear stress, and the change in pore pressure (PP).

20 MPa, shear bands propagate outwards, embedded in a plasticized domain which is nearly circular around the chamber (Figure 9a). An increase in internal pressure increases the radius of this plasticized domain. In order to compare this result with the other two codes Adeli and Flac^{3D}, we note that a state of lithostatic fluid pore pressure produces the same effect on failure as simply removing the gravity force. The results obtained with Adeli and with Flac^{3D} thus simply have gravity switched off, and are displayed in Figures 9b and 9c. The fractured domain, the strain and stress distributions between all three codes compare well, despite the obvious differences due to variable mesh resolutions.

[69] It is delicate to simulate the occurrence of mode I failure using a continuum mesh, but *White et al.* [2004] showed that FLAC methods were able at least to correctly identify domains of mode I failure. *Gerbault* [2012] considered a one-way coupling model at lithostatic pore fluid pressure and a tensile strength T = 5 MPa. In this model (not shown here), tensile failure indeed begins at the chamber wall at ΔP = 8.6 MPa [*Gerbault*, 2012]. Note that this specific situation finally corresponds to usual assumptions of mode I opening for an overpressure of the order of 10 MPa.

5.3. Two-Way Coupling and Initial Lithostatic Pore Fluid Pressure (M7)

[70] A last comparison is presented here to benchmark the previous series of models M6, in which a lithostatic pore fluid pressure ratio controls the onset of failure with a one-way coupling. Here, two-way coupling is tested using FLAC^{3D}, with an initial state of lithostatic fluid pore pressure and an internal overpressure ΔP = 20 MPa. Results shown in Figure 10 compare with those displayed in Figure 9:

[71] 1. At high porosity with n_0 = 0.1 (Figure 10a, M7), the domain of failure around the chamber wall

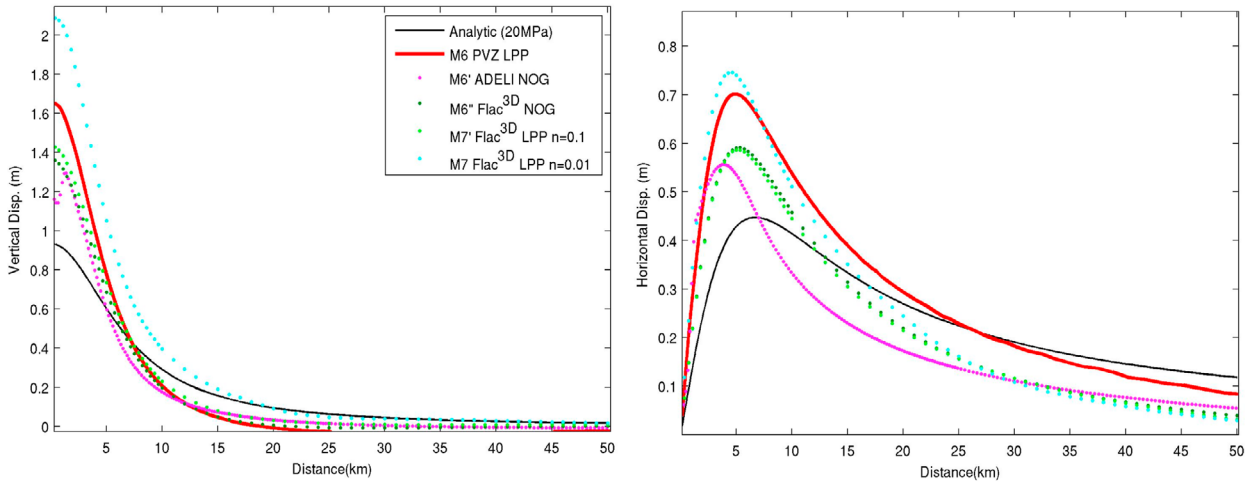

Figure 11. (left) Vertical and (right) horizontal displacements for $\Delta P = 20$ MPa, simulating a case of lithostatic bedrock fluid pressure (models M6 and M7). M6 model with Parovoz assumes failure for a lithostatic state of pore pressure (LPP), while Adeli and the first of the Flac^{3D} models exclude gravity (models M6′ and M6″). The two hydromechanical models M7 and M7′ with Flac^{3D} test the effect of $n = 0.01$ and $n = 0.1$.

adopts an "ear" shape similar to that obtained in models M6. It is associated to an increase in bedrock fluid pressure $\Delta p_f = 2.7$ MPa (Figure 10a, rightmost plot).

[72] 2. At low porosity ($n_0 = 0.01$, model M7′, Figure 10b), shear failure expands around the chamber wall (~100 m wide), and the ear tips expanding upwards are close to connecting to the surface. This effect is due to the reduction of the original pore space (i.e., porosity) with deformation, resulting from the chamber load. The change in fluid pressure reaches a maximum $\Delta p_f = 9.9$ MPa, which is sufficient to decrease the effective stress and trigger rock failure.

[73] Thus, in a fluid-saturated bedrock of low porosity, a factor 3 increase in fluid pressure (Δp_f) can trigger the propagation of a large plastic domain, and perhaps even cause an eruption. In contrast, a dry and porous bedrock would not fail anywhere.

[74] The modeled ground surface displacements are shown in Figure 11, for all models M6 and M7 that simulate a situation of bedrock at lithostatic pore fluid pressure:

[75] 1. Large differences of about 30% are observed between the Parovoz model M6 ($\max(U_y) = 1.65$ m) and the Adeli model M6′ ($\max(U_y) = 1.3$ m), once more due to the presence of an elastic chamber in the former case, and a more "rigid" yield criterion in the latter case. The Flac^{3D} model (M6″) produces intermediate values (see Table 2). Also, horizontal displacement affects a narrower domain in model M6′. These results confirm those from section 4.4, that once the plasticized domains dominate over the elastic domains around the chamber, little differences in overpressures are sufficient to explain large differences in surface uplift.

[76] 2. Displacements are also sensitive to initial rock porosity, with a difference in maximum vertical uplift of 0.7 m (about 30% again) between the high and low porosity models (Figure 11). Surface deformation decreases when porosity increases, due to the absorption of "stress-induced strain" in elastic pores. This result illustrates how variations in pore fluid pressure produce additional deformation of the ground surface given the internal overpressure. We conclude that variations in bedrock pore fluid pressure significantly affect surface displacements above an active volcano.

6. Discussion and Conclusion

[77] The onset and propagation of failure from a magmatic reservoir is often considered in terms of the propagation of dikes and sills opening from preexisting magma-filled cracks [e.g., *Rubin and Pollard*, 1987; *Lister and Kerr*, 1991; *Rubin*, 1993, 1995; *McLeod and Tait*, 1999; *Fialko et al.*, 2001; *Marti et al.*, 2008], and has led to the paradigm that failure occurs as soon as the internal overpressure ΔP reaches values of the order of the bedrock tensile strength T. However, for this condition to be valid, the initial magmatic overpressure (ΔP) must be distributed at the chamber's wall along a radial "thin zone" representing the pre-

opened crack. Appropriate conditions that inhibit both the existence of a viscous shell around the chamber or the freezing of incipient dikes must also be satisfied [e.g., *Rubin*, 1995; *Karlstrom et al.*, 2010]. An appropriate geometrical representation of the boundaries of a magma reservoir results from several properties that determine whether propagation of failure from a pre-existing magma-filled crack is a more valid approximation than that of fault nucleation in intact bedrock. Field observations seem to illustrate the occurrence of both mechanisms with either mode I opening structures (e.g., see review by *Gudmundsson* [2006]), or shear failure preceding dike formation [*Woodcock and Underhill*, 1987; *Henry et al.*, 1997; *White et al.*, 2011]. When considering this second view-point, *Gerbault* [2012] showed that shear failure occurs rather than tensile failure at the walls of an inflating chamber, and at an internal overpressure significantly greater than the usually inferred limit given by the rocks tensile strength (similar to the result obtained when tensile failure alone was considered [*Grosfils*, 2007]). Both view-points merge when one considers a bedrock that is already at a state of lithostatic pore fluid pressure, since the effect of gravity is effectively suppressed, and tensile failure is enabled for low overpressures of the order of the tensile strength [e.g., *Rozhko et al.*, 2007]. The present study has developed some aspects of this second view-point.

[78] One may argue that the gravity body force may be neglected when one is only interested in a "relative approach" that considers departure from an equilibrium state. However, as long as even the effective stress used to assess fracturing remains tied to a yield criterion that depends on the mean pressure, it remains necessary to account for the gravity body force. Only in the very specific case where the bedrock is saturated of fluids in pores (and the effective mean stress is zero), do conditions for tensile rupture become independent from the mean stress, and thus from gravity.

[79] Here, we have detailed the benchmarking issues of elasto-plastic solutions, and illustrated the results with a variety of tests including another H/R ratio, the application of underpressure, and the incorporation of hydromechanical coupling. In summary, about 30% of uncertainty in surface displacements can be attributed to elasto-plastic behavior, and another 30% to hydromechanical effects. For example, in comparison to the discussion by *Battaglia et al.* [2003] on the importance of magmatic sources fitting both vertical and horizontal surface displacements, our elasto-plastic solutions suggest that the use of elastic solutions may be more judicious if fitting distant "slopes" (around 2 to 4 H) rather than values immediately above the center of the source (which can be greatly amplified by localized failure deformation, i.e., as also obtained by *Trasatti et al.* [2005]).

[80] Additional results are as follows:

[81] 1. The analytical expression for the vertical and horizontal displacements at the surface in plane-strain is given (equation (2) had not been published to our knowledge). While elastic solutions are all consistent in between the three numerical codes that we used, they remain valid only until Stage 3, i.e., as long as the plastic domain is not connected between the chamber and the surface. Then, elasto-plastic numerical solutions differ for several reasons. One code includes an elastic chamber, and another code uses a Drucker-Prager formulation for failure. Differences in strain localization are also due to mesh resolution, a problem which has been extensively studied in engineering mechanics [e.g., *Prevost and Loret*, 1990]. Here, high resolution shear bands are obtained thanks to a very high mesh resolution, and they compare with potential slip-lines solutions derived for tunneling engineering. We make a call to the community to extend our benchmark results linking internal pressure and localized failure patterns. Note that we have been considering here the onset of failure and its propagation in a continuum. At large cumulated strain and as the domain becomes largely plastified, we expect that with the rise of discontinuity, failure zones adopt a more direct pattern of vertical faults linking the chamber to the surface (e.g., the difference between "elastic" and "plastic" solutions [*Gerbault et al.*, 1998]).

[82] 2. Models that account for hydromechanical coupling show that the initial porosity of rocks influences the extent of the failure domain, its shape, and the magnitude of displacements and stresses at the surface. It is well known that changes in fluid pressure can trigger failure, and fluid pressurization has frequently been observed in volcanic systems [*Bjornsson et al.*, 1990; *Watanabe*, 1983; *Reid*, 2004; *Segall*, 2009; *Sturkell et al.*, 2006; *White et al.*, 2011]. However, to our knowledge, the effects shown here of coupling between fluid pressure, deformation and hydraulic properties around a magma chamber, and their influence on the propagation of failure, had not been clearly documented before. Low porosity bedrocks saturated with fluids in pores is very prone to fail for small internal magma overpressure. Consequently, geodetic studies

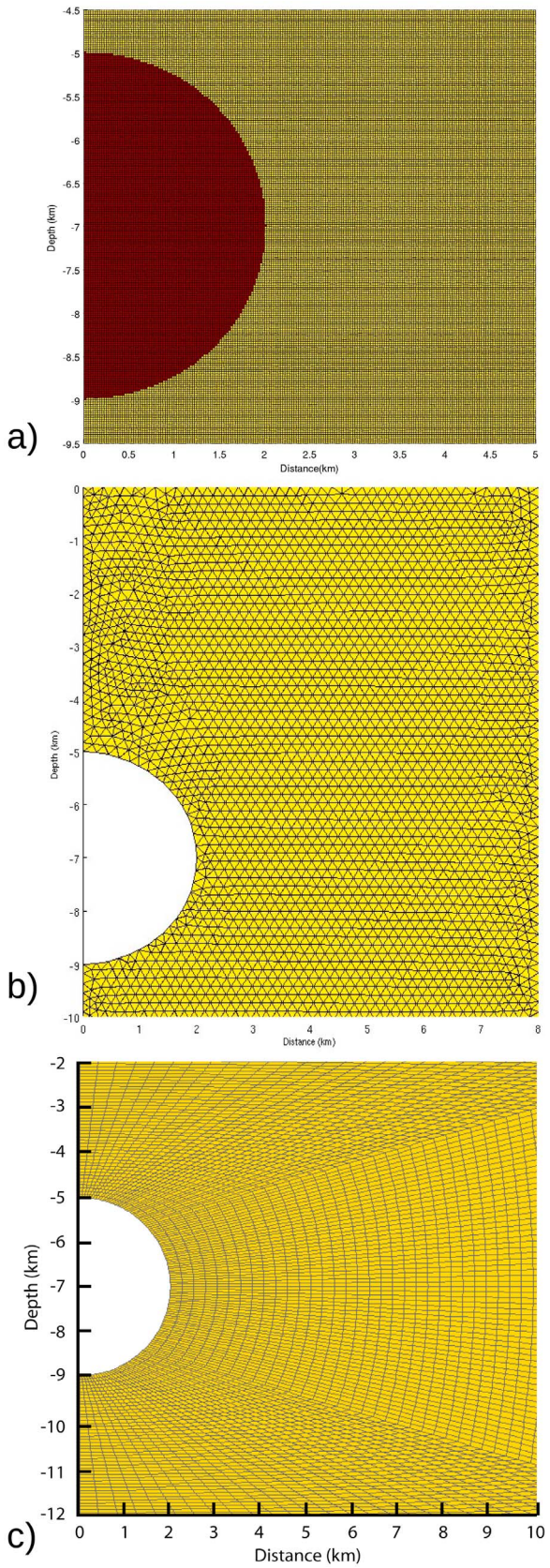

that use standard elastic solutions to evaluate chamber depth and radius should not be surprised if their data fit is sometimes associated to "high" overpressures [e.g., *Bonaccorso et al.*, 2005], all the more if the surrounding bedrock contains saturated low porosity rocks. It is therefore useful to be able to assess the hydromechanical properties of the bedrock [e.g., *Heap et al.*, 2011].

[83] In the literature, geodetic measurements of ground surface displacements rarely exceed one meter above inflating volcanic sources. Volcanological observations of relatively small surface displacements may be associated to small influxes of magma that trigger failure and dike intrusion, and inhibit the occurrence of large eruptions, in a commonly saturated fluid-pore pressure bedrock. The fact that we obtain several meters of uplift (yet given a large 7 km depth and 2 km radius source) indicates that our modeled plastic effects may in fact represent an end point achieved only sometimes in nature, when low porosity and hydrostatic pore fluid pressure conditions prevail in a sufficiently homogeneous bedrock. For instance, *Mogi* [1958] cited leveling values reaching an uplift of 3.96 m and horizontal displacements of 1.3 m above Kilauea shield volcano during the period 1912–1927, We also recall that *Wegler et al.* [2006] interpreted the evolution of seismic wave speeds at Merapi volcano as resulting from continuous pressure increase in between two eruptions, indicating that a single eruption may not necessarily release the building up of internal overpressure.

[84] On the other hand, the temporal evolution of bedrock pore pressure, for example due to meteoritic or glacial water infiltration, or in contrast due to cementation, may also allow to consider transitions from one end-member to the other as an explanation of the historical evolution of specific volcanic areas. The following potential scenario may be interesting to consider: porosity reduction in response to cementation, added to the arrival of meteoritic fluids, may cause a volcanic system to evolve from a stable situation at hydrostatic bedrock pore pressure and relatively high internal overpressures, to an unstable situation of near-lithostatic pore pressure. A large eruption may then be triggered, despite no significant increase of the internal overpressure.

Figure A1. Meshes used in the three codes: (a) quadrilaterals for Parovoz, which includes the chamber in the mesh, (b) a mesh of triangles for Adeli, and (c) a radial mesh of quadrilaterals for FLAC^{3D}.

[85] A number of complementary analyses are open for the future, by associating our elasto-plastic and hydromechanical approach with numerous and already well identified other factors. Non-circular magma chamber geometries (i.e., ellipsoïdal), multiple chambers, elastic heterogeneity and a volcanic edifice [i.e., *Pinel and Jaupart*, 2003; *Gudmundsson*, 2006; *Masterlark*, 2007; *Segall*, 2009; *Long and Grosfils*, 2009] are necessary to account for in order to proceed to proper comparison with natural three-dimensional cases. Incorporation of more realistic rheologies including temperature-dependent viscosity [e.g., *Dragoni and Magnanensi*, 1989; *Bonaccorso et al.*, 2005; *Karlstrom et al.*, 2010] and lithospheric flexure [*Galgana et al.*, 2011] introduces additional controls on failure mechanisms. Hydromechanical processes deserve a more elaborated approach, including poro-elastic effects [*Bonafede and Mazzanti*, 1998; *Hutnak et al.*, 2009]. Finally, application of a dilatational deformation instead of overpressure may be more sensible to fit models to measurements above active volcanoes. The complex multiphase processes inside a chamber may also lead to non-negligible inhomogeneous chamber growth.

Appendix A

[86] Figure A1 illustrates the meshes defined in each three codes, zoomed around the circular chamber: quadrilaterals for Parovoz and which includes the chamber in the mesh, a mesh of triangles for Adeli, and a radial mesh of quadrilaterals for FLAC^{3D}.

Acknowledgments

[87] M.G. thanks J. Salençon and M. Sakellariou for sharing their knowledge of engineering plasticity, E. Holohan and E. Grosfils for many very good volcanological advices, and A. Rubin for sharing his views on dike propagation. N. Croiset co-explored preliminary models with M.G., and her work is acknowledged (N. Croiset, Master's report, ENS Lyon, Lyon, France, 2007). J. Giannetti helped with the library investigations and M. Testi with Matlab visualization. The Editor J. Tyburczy and reviewers are sincerely thanked for their very constructive comments, which improved the value of this work.

References

Acocella, V. (2007), Understanding caldera structure and development: An overview of analogue models compared to natural calderas, *Earth Sci. Rev.*, *85*, 125–160, doi:10.1016/j.earscirev.2007.08.004.

Anderson, E. M. (1936), The dynamics of formation of cone-sheets, ring-dykes and cauldron subsidences, *Proc. R. Soc. Edinburgh*, *56*, 128–163.

Battaglia, M., P. Segall, and C. Roberts (2003), The mechanics of unrest at Long Valley Caldera: 2. Constraining the nature of the source using geodetic and micro-gravity data, *J. Volcanol. Geotherm. Res.*, *127*, 219–245, doi:10.1016/S0377-0273(03)00171-9.

Bjornsson, G., L. Kristjansson, and H. Johnsen (1990), Some observations of the Heimaey deep drill hole during the eruption of 1973, *Jokull*, *26*, 52–57.

Bonaccorso, A., S. Cianetti, C. Giunchi, E. Trasatti, M. Bonafede, and E. Boschi (2005), Analytical and 3-D numerical modeling of Mt. Etna (Italy) volcano inflation, *Geophys. J. Int.*, *163*, 852–862, doi:10.1111/j.1365-246X.2005.02777.x.

Bonafede, M., and C. Ferrari (2009), Analytical models of deformation and residual gravity changes due to a Mogi source in a viscoelastic medium, *Tectonophysics*, *471*, 4–13, doi:10.1016/j.tecto.2008.10.006.

Bonafede, M., and M. Mazzanti (1998), Modelling gravity variations consistent with ground deformation in the Campi Flegrei caldera (Italy), *J. Volcanol. Geotherm. Res.*, *81*, 137–157.

Bower, S. M., and A. W. Woods (1997), control of magma volatile content and chamber depth on the mass erupted during explosive volcanic eruptions, *J. Geophys. Res.*, *102*, 10,273–10,290, doi:10.1029/96JB03176.

Burov, E., and L. Guillou-Frottier (1999), Thermomechanical behavior of large ash flow calderas, *J. Geophys. Res.*, *104*(B10), 23,081–23,109, doi:10.1029/1999JB900227.

Burov, E., C. Jaupart, and L. Guillou-Frottier (2003), Ascent and emplacement of buoyant magma bodies in brittle-ductile upper crutst, *J. Geophys. Res.*, *108*(B4), 2177, doi:10.1029/2002JB001904.

Caquot, A., and J. Kerisel (1956), *Traité de Mécanique des Sols*, Gauthier-Villars, Paris.

Cayol, V., and F. H. Cornet (1998), Three-dimensional modeling of the 1983–1984 eruption at piton de la Fournaise volcanoe, Réunion Island, *J. Geophys. Res.*, *103*(B8), 18,025–18,037, doi:10.1029/98JB00201.

Chéry, J., A. Bonneville, J. P. Villote, and D. Yuen (1991), Numerical modelling of caldera dynamical behaviour, *Geophys. J. Int.*, *105*, 365–379, doi:10.1111/j.1365-246X.1991.tb06719.x.

Chéry, J., M. D. Zoback, and R. Hassani (2001), An integrated mechanical model of the San Andreas fault in central and northern California, *J. Geophys. Res.*, *106*, 22,051–22,066, doi:10.1029/2001JB000382.

Cundall, P. A. (1989), Numerical experiments on localization in frictional materials, *Arch. Appl. Mech.*, *59*, 148–159, doi:10.1007/BF00538368.

Cundall, P., and M. Board (1988), A microcomputer program for modeling large-strain plasticity problems, in *Numerical Methods in Geomechanics*, pp. 2101–2108, A. A. Balkema, Rotterdam, Netherlands.

d'Escatha, Y., and J. Mandel (1974), Stabilité d'une galerie peu profonde en terrain meuble, *Extrait Ind. Miner., Numero Spec.*, *1974*, 45–53.

Dieterich J. H., and R. W. Decker (1975), Finite element modeling of surface deformation associated with volcanism, *J. Geophys. Res.*, *80*, 4094–4102.

Dragoni, M., and C. Magnanensi (1989), Displacements and stress produced by a pressurised spherical magma chamber, surrounded by a viscoelastic shell, *Phys. Earth Planet. Inter.*, *56*, 316–328, doi:10.1016/0031-9201(89)90166-0.

Engelder, T., and J. T. Leftwich (1997), A pore-pressure limit in overpressured South Texas oil and gas field, in *Seals, Traps, and the Petroleum System*, edited by R. C. Surdam, *AAPG Mem.*, *67*, 255–267.

Fialko, Y., Y. Khazan, and M. Simons (2001), Deformation due to a pressurized horizontal circular crack in an elastic half-space, with applications to volcano geodesy, *Geophys. J. Int.*, *146*, 181–190, doi:10.1046/j.1365-246X.2001.00452.x.

Galgana, G. A., P. J. McGovern, and E. B. Grosfils (2011), Evolution of large Venusian volcanoes: Insights from coupled models of lithospheric flexure and magma reservoir pressurization, *J. Geophys. Res.*, *116*, E03009, doi:10.1029/2010JE003654.

Gerbault, M. (2012), Pressure conditions for shear and tensile failure around a circular magma chamber, insight from elasto-plastic modeling, in *Faulting, Fracturing and Igneous Intrusion in the Earth's Crust*, edited by D. Healy, *Geol. Soc. Spec. Publ.*, in press.

Gerbault, M., A. Poliakov, and M. Daignières (1998), Prediction of faulting from the theories of elasticity and plasticity: What are the limits?, *J. Struct. Geol.*, *20*, 301–320, doi:10.1016/S0191-8141(97)00089-8.

Gray, J. P., and J. J. Monaghan (2004), Numerical modelling of stress fields and fracture around magma chambers, *J. Volcanol. Geotherm. Res.*, *135*, 259–283, doi:10.1016/j.jvolgeores.2004.03.005.

Grosfils, E. B. (2007), Magma reservoir failure on the terrestrial planets: Assessing the importance of gravitational loading in simple elastic models, *J. Volcanol. Geotherm. Res.*, *166*, 47–75, doi:10.1016/j.jvolgeores.2007.06.007.

Gudmundsson, A. (1988), Effect of tensile stress concentration around magma chambers on intrusion and extrusion frequencies, *J. Volcanol. Geotherm. Res.*, *35*, 179–194, doi:10.1016/0377-0273(88)90015-7.

Gudmundsson, A. (2006), How local stresses control magma-chamber ruptures, dyke injections, and eruptions in composite volcanoes, *Earth Sci. Rev.*, *79*, 1–31, doi:10.1016/j.earscirev.2006.06.006.

Gudmundsson, A., J. Marif, and E. Turon (1997), Stress field generating ring faults in volcanoes, *Geophys. Res. Lett.*, *24*, 1559–1562, doi:10.1029/97GL01494.

Gudmundsson, A., I. Fjeldskaar, and S. L. Brenner (2002), Propagation pathways and fluid transport of hydrofractures in jointed and layered rocks in geothermal fields, *J. Volcanol. Geotherm. Res.*, *116*, 257–278, doi:10.1016/S0377-0273(02)00225-1.

Guillou-Frottier, L., E. B. Burov, and J. P. Milesi (2000), Genetic links between ash flow calderas and associated ore deposits as revealed by large-scale thermo-mechanical modeling, *J. Volcanol. Geotherm. Res.*, *102*, 339–361, doi:10.1016/S0377-0273(00)00246-8.

Hardy, S. (2008), Structural evolution of calderas: Insights from two-dimensional discrete element formulations?, *Geology*, *36*, 927–930, doi:10.1130/G25133A.1.

Hassani, R., D. Jongmans, and J. Chéry (1997), Study of plate deformation and stress in subduction processes using two-dimensional numerical models, *J. Geophys. Res.*, *102*, 17,951–17,965, doi:10.1029/97JB01354.

Heap, M. J., P. Baud, P. G. Meredith, S. Vinciguerra, A. F. Bell, and I. G. Main (2011), Brittle creep in basalt and its application to time-dependent volcano deformation, *Earth Planet. Sci. Lett.*, *307*, 71–82, doi:10.1016/j.epsl.2011.04.035.

Henry, C. D., M. J. Kunk, W. R. Muehlberger, and W. C. McIntosh (1997), Igneous evolution of a complex laccolith-caldera, the Solitario, Trans-Pecos Texas: Implications for calderas and subjacent plutons, *Geol. Soc. Am. Bull.*, *109*, 1036–1054, doi:10.1130/0016-7606(1997)109<1036:IEOACL>2.3.CO;2.

Hillis, R. R. (2003), Pore pressure/stress coupling and its implications for rock failure, *Geol. Soc. Spec. Publ.*, *216*, 359–368, doi:10.1144/GSL.SP.2003.216.01.23.

Hubbert, M. K., and W. W. Rubey (1959), Role of fluid pressure in mechanics of overthrust faulting, *Geol. Soc. Am. Bull.*, *70*, 115–166, doi:10.1130/0016-7606(1959)70[115:ROFPIM]2.0.CO;2.

Huppert, H., and A. W. Woods (2002), The role of volatiles in magma chamber dynamics, *Nature*, *420*, 493–495, doi:10.1038/nature01211.

Hurwitz, S., L. B. Christiansen, and P. A. Hsieh (2007), Hydrothermal fluid flow and deformation in large calderas: Inferences from numerical simulations, *J. Geophys. Res.*, *112*, B02206, doi:10.1029/2006JB004689.

Hutnak, M., S. Hurwitz, S. E. Ingebritsen, and P. A. Hsieh (2009), Numerical models of caldera formation: Effects of multiphase and multicomponent hydrothermal fluid flow, *J. Geophys. Res.*, *114*, B04411, doi:10.1029/2008JB006151.

Itasca Consulting Group (2006), FLAC^{3D}, Fast Lagrangian Analysis of Continua in 3 Dimensions, version 3.0, user manual, Minneapolis, Minn.

Jeffery, J. B. (1921), Plane stress and plane strain in bi-polar coordinates, *Philos. Trans. R. Soc. London A*, *221*, 265–293, doi:10.1098/rsta.1921.0009.

Jellinek, A. M., and D. J. De Paolo (2003), A model for the origin of large silicic magma chambers: precursors of caldera-forming eruptions, *Bull. Volcanol.*, *65*, 363–381.

Johnson, D. J., F. Sigmundsson, and P. T. Delaney (2000), Comment on "Volume of magma accumulation or withdrawal estimated from surface uplift or subsidence, with application to the 1960 collapse of Kilauea volcano" by P. T. Delaney and D. F. McTigue, *Bull. Volcanol.*, *61*, 491–493.

Karlstrom, L., J. Dufek, and M. Manga (2010), Magma chamber stability in arc and continental crust, *J. Volcanol. Geotherm. Res.*, *190*(3–4), 249–270, doi:10.1016/j.jvolgeores.2009.10.003.

Kaus, B. (2010), Factors that control the angle of shear bands in geodynamic numerical models of brittle deformation, *Tectonophysics*, *484*, 36–47, doi:10.1016/j.tecto.2009.08.042.

Kumagai, H., P. Placios, M. Ruiz, H. Yepes, and T. Kozono (2011), Ascending seismic source during an explosive eruptionat Tunguruhua volcano, Ecuador, *Geophys. Res. Lett.*, *38*, L01306, doi:10.1029/2010GL045944.

Kusumoto, S., and K. Takemura (2003), Numerical simulation of caldera formation due to collapse of a magma chamber, *Geophys. Res. Lett.*, *30*(24), 2278, doi:10.1029/2003GL018380.

Lavier, L., W. Buck, and A. Poliakov (2000), Factors controlling normal fault in an ideal brittle layer, *J. Geophys. Res.*, *105*, 23,431–23,442, doi:10.1029/2000JB900108.

Lister, J. R., and R. C. Kerr (1991), Fluid-mechanical models of crack propagation and their application to magma transport in dykes, *J. Geophys. Res.*, *96*, 10,049–10,077, doi:10.1029/91JB00600.

Long, S. M., and E. B. Grosfils (2009), Modeling the effect of layered volcanic material on magma reservoir failure and

associated deformation, with application to Long Valley caldera, California, *J. Volcanol. Geotherm. Res.*, *186*, 349–360, doi:10.1016/j.jvolgeores.2009.05.021.

Marti, J., A. Geyer, A. Folch, and J. Gottsmann (2008), A review of collapse caldera modelling, in *Caldera Volcanism: Analysis, Modelling and Response*, *Dev. Volcanol.*, vol. 10, pp. 233–283, Elsevier, Amsterdam, doi:10.1016/S1871-644X(07)00006-X.

Masek, J. G., and C. C. Duncan (1998), Minimum-work mountain building, *J. Geophys. Res.*, *103*, 907–917, doi:10.1029/97JB03213.

Massinas, S. A., and M. G. Sakellariou (2009), Closed-form solution for a plastic zone formation around a circular tunnel in half-space obeying Mohr-Coulomb criterion, *Geotechnique*, *59*(8), 691–701, doi:101680/geot8.069.

Masterlark, T. (2007), Magma intrusion and deformation predictions: Sensitivities to the Mogi assumptions, *J. Geophys. Res.*, *112*, B06419, doi:10.1029/2006JB004860.

McLeod, P., and S. Tait (1999), The growth of dyke from magma chambers, *J. Volcanol. Geotherm. Res.*, *92*, 231–245, doi:10.1016/S0377-0273(99)00053-0.

McTigue, D. F. (1987), Elastic stress and deformation near a finite spherical magma body: Resolution of a point source paradox, *J. Geophys. Res.*, *92*, 12,931–12,940, doi:10.1029/JB092iB12p12931.

Mogi, K. (1958), Relations between the eruption of various volcanoes and the deformation of the ground surfaces around them, *Bull. Earthquake Res. Inst. Univ. Tokyo*, *36*, 99–134.

Nadai, A. (1950), *The Theory of Flow and Fracture of Solids*, 402 pp., Mc-Graw Hill, New York.

Parfitt, E. A., L. Wilson, and J. W. Head (1993), Basaltic magma reservoirs: Factors controlling their rupture characteristics and evolution, *J. Volcanol. Geotherm. Res.*, *55*, 1–14, doi:10.1016/0377-0273(93)90086-7.

Pinel, V., and C. Jaupart (2003), Magma chamber behavior beneath a volcanic edifice, *J. Geophys. Res.*, *108*(B2), 2072, doi:10.1029/2002JB001751.

Pinel, V., and C. Jaupart (2005), Caldera formation by magma withdrawal from a reservoir beneath a volcanic edifice, *Earth Planet. Sci. Lett.*, *230*, 273–287, doi:10.1016/j.epsl.2004.11.016.

Podladchikov, Y., A. N. B. Poliakov, and P. Cundall (1993), An explicit inertial method for the simulation of visco-elastic flow: An evaluation of elastic effects on diapiric flow in two- and three-layers models, in *Flow and Creep in the Solar System: Observation, Modelling and Theory*, *NATO Sci. Ser., Ser. C*, vol. 391, pp. 175–195, Kluwer Acad., Dordrecht, Netherlands.

Poliakov, A., and Y. Podladchikov (1992), Diapirism and topography, *Geophys. J. Int.*, *109*, 553–564, doi:10.1111/j.1365-246X.1992.tb00117.x.

Poliakov, A. N. B., Y. Podladchikov, and C. Talbot (1993), Initiation of salt diapirs with frictional overburdens: Numerical experiments, *Tectonophysics*, *228*, 199–210.

Prevost, J. H., and B. Loret (1990), Dynamic strain localization in elasto-(visco-)plastic solids, part 2. Plane Strain examples, *Comput. Methods Appl. Mech. Eng.*, *83*, 275–294, doi:10.1016/0045-7825(90)90074-V.

Pritchard, M. E., and M. Simons (2004), An InSAR-based survey of volcanic deformation in the central Andes, *Geochem. Geophys. Geosyst.*, *5*, Q02002, doi:10.1029/2003GC000610.

Reid, M. E. (2004), Massive collapse of volcano edifices triggered by hydrothermal pressurization, *Geology*, *32*(5), 373–376, doi:10.1130/G20300.1.

Rivalta, E., and P. Segall (2008), Magma compressibility and the missing source for some dike intrusions, *Geophys. Res. Lett.*, *35*, L04306, doi:10.1029/2007GL032521.

Roche, O., and T. H. Druitt (2001), Onset of caldera collapse during ignimbrite eruptions, *Earth Planet. Sci. Lett.*, *191*, 191–202, doi:10.1016/S0012-821X(01)00428-9.

Rozhko, A. Y., Y. Y. Podladchikov, and F. Renard (2007), Failure patterns caused by localized rise in pore-fluid overpressure and effective strength of rocks, *Geophys. Res. Lett.*, *34*, L22304, doi:10.1029/2007GL031696.

Rubin, A. M. (1993), Dikes vs. Diapirs in viscoleastic rock, *Earth Planet. Sci. Lett.*, *119*, 641–659, doi:10.1016/0012-821X(93)90069-L.

Rubin, A. M. (1995), Propagation of magma-filled cracks, *Annu. Rev. Earth Planet. Sci.*, *23*, 287–336, doi:10.1146/annurev.ea.23.050195.001443.

Rubin, A. M., and D. D. Pollard (1987), Origins of blade-like dikes in volcanic rift zones, *U.S. Geol. Surv. Prof. Pap.*, *1350*, 1449–1470.

Sammis, C. G., and B. R. Julian (1987), Fracture instabilities accompanying dike intrusions, *J. Geophys. Res.*, *92*, 2597–2605, doi:10.1029/JB092iB03p02597.

Sartoris, G., J. P. Pozzi, C. Philippe, and J. L. le Mouel (1990), Mechanical instability of shallow magma chambers, *J. Geophys. Res.*, *95*, 5141–5151, doi:10.1029/JB095iB04p05141.

Segall, P. (2009), *Earthquake and Volcano Deformation*, 432 pp., Princeton Univ. Press, Princeton, N. J.

Sturkell, E., F. Sigmundsson, and R. Slunga (2006), 1983–2003 decaying rate of deflation at Askja caldera: Pressure decrease in an extensive magma plumbing system at a spreading plate boundary, *Bull. Volcanol.*, *68*, 727–735, doi:10.1007/s00445-005-0046-1.

Tait, S., C. Jaupart, and S. Vergniolle (1989), Pressure, gas content and eruption periodicity of a shallow, crystallizing magma chamber, *Earth Planet. Sci. Lett.*, *92*, 107–123, doi:10.1016/0012-821X(89)90025-3.

Timoshenko, S., and J. N. Goodier (1970), *Theory of Elasticity*, 2nd ed., 608 pp., McGraw-Hill, New York.

Townend, J., and M. D. Zoback (2000), How faulting keeps the crust strong, *Geology*, *28*, 399–402, doi:10.1130/0091-7613(2000)28<399:HFKTCS>2.0.CO;2.

Trasatti, E., C. Giunchu, and M. Bonafede (2005), Structural and rheological constraints on source depth and overpressure estimates at the Campi Flegrei caldera, Italy, *J. Volcanol. Geotherm. Res.*, *144*, 105–118, doi:10.1016/j.jvolgeores.2004.11.019.

Turcotte, D., and G. Schubert (1982), *Geodynamics, Applications of Continuum Physics to Geological Problems*, 450 pp., Wiley, New York.

Vermeer, P. A., and R. de Borst (1984), Non-associated plasticity for soils, concrete and rocks, *Heron*, *29*, 1–75.

Verruijt, A. (1998), Deformations of an elastic half plane with a circular cavity, *Int. J. Solids Struct.*, *35*(21), 2795–2804, doi:10.1016/S0020-7683(97)00194-7.

Watanabe, H. (1983), Changes in water level and their implications to the 1977–1978 activity of Usu volcano, in *Arc Volcanism: Physics and Tectonics*, edited by D. Shimozuru and I. Yokoyama, pp. 81–93, Terra Sci., Tokyo.

Wegler, U., B.-G. Lühr, R. Snieder, and A. Ratdomopurbo (2006), Increase of shear wave velocity before the 1998 eruption of Merapi volcano (Indonesia), *Geophys. Res. Lett.*, *33*, L09303, doi:10.1029/2006GL025928.

White, B. G., M. K. Larson, and S. R. Iverson (2004), Origin of mining-induced fractures through macro-scale distortion, in *Gulf Rocks 2004: Rock Mechanics Across Borders and*

Disciplines, Proceedings of the Sixth North American Rock Mechanics Conference, Houston, Texas, pp. 1–8, Am. Rock Mech. Assoc., Alexandria, Va.

White, R. S., J. Drew, H. R. Martens, J. Key, H. Soosalu, and S. S. Jakobsdottir (2011), Dynamics of dyke intrusion in the mid-crust of Iceland, *Earth Planet. Sci. Lett.*, *304*, 300–312, doi:10.1016/j.epsl.2011.02.038.

Woodcock, N. H., and R. J. Underhill (1987), Emplacement-related fault patterns around the Northern granite, Arran, Scotland, *Geol. Soc. Am. Bull.*, *98*, 515–527, doi:10.1130/0016-7606(1987)98<515:EFPATN>2.0.CO;2.